

# A Candidate Young Massive Planet in Orbit around the Classical T Tauri Star CI Tau<sup>1</sup>

Christopher M. Johns-Krull<sup>2,3</sup>, Jacob N. McLane<sup>4,5</sup>, L. Prato<sup>3,4</sup>, Christopher J. Crockett<sup>3,6</sup>, Daniel T. Jaffe<sup>7</sup>, Patrick M. Hartigan<sup>2</sup>, Charles A. Beichman<sup>8,9</sup>, Naved I. Mahmud<sup>2</sup>, Wei Chen<sup>2</sup>, B. A. Skiff<sup>4</sup>, P. Wilson Cauley<sup>2,10</sup>, Joshua A. Jones<sup>2</sup>, G. N. Mace<sup>7</sup>

## ABSTRACT

The  $\sim 2$  Myr old classical T Tauri star CI Tau shows periodic variability in its radial velocity (RV) variations measured at infrared (IR) and optical wavelengths. We find that these observations are consistent with a massive planet in a  $\sim 9$ -day period orbit. These results are based on 71 IR RV measurements of this system obtained over 5 years, and on 26 optical RV measurements obtained over 9 years. CI Tau was also observed photometrically in the optical on 34 nights over  $\sim$ one month in 2012. The optical RV data alone are inadequate to identify an orbital period, likely the result of star spot and activity induced noise for this relatively small dataset. The infrared RV measurements reveal significant periodicity at  $\sim 9$

---

<sup>1</sup>This paper includes data taken at The McDonald Observatory of The University of Texas at Austin.

<sup>2</sup>Department of Physics and Astronomy, Rice University, MS-108, 6100 Main Street, Houston, TX 77005, USA

<sup>3</sup>Visiting Astronomer at the Infrared Telescope Facility, which is operated by the University of Hawaii under cooperative agreement NCC 5-538 with the National Aeronautics and Space Administration, Office of Space Science, Planetary Astronomy Program.

<sup>4</sup>Lowell Observatory, 1400 West Mars Hill Rd. Flagstaff, AZ 86001, USA; jmclane@lowell.edu, lprato@lowell.edu

<sup>5</sup>Department of Physics & Astronomy, Northern Arizona University, S San Francisco Street, Flagstaff, AZ 86011, USA

<sup>6</sup>Science News, 1719 N St NW, Washington, DC 20036, USA

<sup>7</sup>Department of Astronomy, University of Texas, R. L. Moore Hall, Austin, TX 78712, USA

<sup>8</sup>Jet Propulsion Laboratory, California Institute of Technology, 4800 Oak Grove Drive, Pasadena, CA 91109, USA

<sup>9</sup>NASA Exoplanet Science Institute (NExSci), California Institute of Technology, 770 S. Wilson Ave, Pasadena, CA 91125, USA

<sup>10</sup>Department of Astronomy, Wesleyan University, 45 Wyllys Avenue, Middletown, CT 06459, USA

days. In addition, the full set of optical and IR RV measurements taken together phase coherently and with equal amplitudes to the  $\sim 9$  day period. Periodic radial velocity signals can in principle be produced by cool spots, hot spots, and reflection of the stellar spectrum off the inner disk, in addition to resulting from a planetary companion. We have considered each of these and find the planet hypothesis most consistent with the data. The radial velocity amplitude yields an  $M \sin i$  of  $\sim 8.1 M_{Jup}$ ; in conjunction with a 1.3 mm continuum emission measurement of the circumstellar disk inclination from the literature, we find a planet mass of  $\sim 11.3 M_{Jup}$ , assuming alignment of the planetary orbit with the disk.

*Subject headings:* planets and satellites: formation – stars: individual (CI Tau) – stars: low-mass – stars: pre-main sequence – starspots – techniques: radial velocities

## 1. Introduction

Exoplanetary systems are common and literally come in all sizes and configurations. These span a parameter space that encompasses more apparently stable arrangements than ever imagined for multi-planet systems, from the hyper-compact KOI-500 (Ragozzine et al. 2012) to the decades- and centuries-long orbits of the HR 8799 planets (Marois et al. 2010), in motion around a vast range of host stars. Intriguingly, however, although exoplanetary systems are found around main sequence stars, post-main sequence giants, brown dwarfs (Chauvin et al. 2004), intermediate age stars (Quinn et al. 2014), and even pulsars (Wolszczan & Frail 1992), to date there are no confirmed radial velocity (RV) detections of exoplanets caught in the act of formation around very young stars.

There are good reasons for this. Stellar systems presumably in the process of forming planets in circumstellar or circumbinary disks are typically located at relatively large distances, i.e.  $>120$  pc. The  $\sim 10$  Myr TW Hya region, at 50 pc, is much closer but contains only a few handfuls of young stars, many, but not all (Bergin et al. 2013), evolved beyond the planet-forming stage (Schneider et al. 2012). Young moving groups near the Sun contain greater numbers of stars but are older yet, and, given their dispersion from their molecular cloud birthplaces, are not only more challenging to age-date, but are also mostly devoid of primordial planet-forming raw materials (Simon et al. 2012). Tantalizingly, directly imaged planets in these moving groups are typically associated with processed debris disks (e.g., Su et al. 2009; Apai et al. 2015), but the planetary bodies themselves have moved well past the formation stage. Thus it is unknown precisely when and at what distances from the parent

star planets form, how rapidly they migrate or are disrupted and/or ejected, and at what age planetary systems acquire stable configurations.

The obstacles to planet surveys around newly-formed stars in the closest regions, such as Ophiuchus and Taurus, are daunting, particularly in the case of classical T Tauri stars (CTTSs), few Myr year old solar analogues with optically thick, actively accreting circumstellar disks. Not only are these stars correspondingly faint, but they are also among the most variable classes of nearby object (Xiao et al. 2012; Stauffer et al. 2014). From relatively mild forms of variability, such as the changes originating from spots on the surface of a rapidly rotating star (e.g., Herbst et al. 2002), to clumpy accretion processes in the presence of strong magnetic fields (Graham 1992; Johns-Krull et al. 1999), to extreme FU Ori behaviors and ideopathic outbursts/dimmings on the order of a visual magnitude or more detected on short time scales (e.g., Fischer et al. 2012; Hillenbrand et al. 2013). In these environments, subtle observations of transits, direct imaging, and RV monitoring are fraught with complications.

Notwithstanding the challenges, impressive progress has been made in the search for young planets, largely through direct imaging studies (Neuhäuser et al. 2005; Luhman et al. 2006; Lafrenière et al. 2008; Schmidt et al. 2008; Ireland et al. 2011; Kraus & Ireland 2012; Delorme et al. 2013; Bowler et al. 2013; Kraus et al. 2014; Sallum et al. 2015). The first putative imaged exoplanet, 2M1207b, was identified as a comoving companion to the substellar M8 dwarf 2M1207 in the TW Hya association (Chauvin et al. 2004, 2005). The LkCa 15 system, located in the younger Taurus region, was imaged using non-redundant masking by Kraus & Ireland (2012) who noted an unusual pattern of near- and mid-infrared (IR) emission in the inner hole of the LkCa 15 transition disk. Several years of observations of LkCa 15 have revealed apparent orbital motion (Ireland & Kraus 2014) and, more recently, apparent accretion (Sallum et al. 2015) onto the candidate protoplanet. Mass estimates for these objects come from comparing their estimated luminosity and temperature with theoretical evolutionary models. However, such models are uncertain at these young ages and the observations required to determine the luminosity and temperature with adequate precision are challenging and yield considerable uncertainty in the final mass estimate for a given object. The companion to GQ Lup (Neuhäuser et al. 2005) has mass estimates that range from  $1 M_{JUP}$  to  $\sim 40 M_{JUP}$  (Neuhäuser et al. 2008). In addition to direct imaging of potential planetary mass companions, some suggestive results have come from transit searches. van Eyken et al. (2012) and Ciardi et al. (2015) observed transits potentially attributable to a planetary mass object in a  $\sim$ half day orbit around a  $< 3$  Myr old T Tauri star in the Orion region, although these results have been called into question by Yu et al. (2015) and Howarth (2016).

The relative lack of confirmed planetary mass companions to very young stars may provide clues to the planet formation process, or may simply be a testament to the difficulty in finding young planets. However, the transformational image of the HL Tau system taken in the recently commissioned long-baseline configuration with ALMA reveals numerous disk gaps highly suggestive of on-going planet formation at a very young age (Partnership, ALMA, Brogan et al. 2015). To fully understand the planet formation and migration process, we will need to identify newly formed planets around these young, difficult targets. This particularly includes looking for close in Jupiter mass and larger companions. Radial velocity surveys have revealed the existence of a brown dwarf desert (e.g., Marcy & Butler 2000), an unexpected paucity of close brown dwarf companions to solar-type stars. It is not yet known if this distribution of secondaries is the result of the formation process itself or the result of evolution. Armitage and Bonnell (2002) suggest that disks massive enough to form brown dwarf companions will be so massive that these companions inevitably interact with the disk, migrate in, and merge with the central star. In this case, close brown dwarf companions may be detected with higher frequency among young stars, particularly those still surrounded by massive disks.

In the last decade our team has undertaken an RV survey of  $\sim 140$  T Tauri stars in the Taurus region to look for signatures of RV variability indicative of young, massive planets in short-period orbits. Although we began our program at McDonald Observatory with high-resolution spectroscopy exclusively at optical wavelengths, we soon added high-resolution IR follow up spectroscopy at the NASA IRTF for candidate confirmation. Visible light line bisector analysis, used to distinguish between the spot and companion origins of RV variability (e.g., Huerta et al. 2008; Prato et al. 2008), is ineffective unless the  $v \sin i$  of the star is significantly greater than the spectrograph resolution element. Thus for a star with  $v \sin i$  values  $< 10 \text{ km s}^{-1}$  and a resolution  $R=60,000$  spectrograph, we obtain at most 4 resolution elements, insufficient for the line bisector analysis (Desort et al. 2007). Because the photosphere-star spot contrast is reduced in the IR, the impact of star spots on IR RV observations is reduced by a factor of at least four in the K band (Mahmud et al. 2011). This serves as a key discriminant between the presence of spots or a planet, which the line bisector analysis failed to provide (Prato et al. 2008). Huélamo et al. (2008) used this approach to show that the suspected planet around TW Hya (Setiawan et al. 2008) was most likely a false signal produced by spots on this rapidly rotating young star.

The current methodology for obtaining relatively high-precision IR RVs requires fitting observed or synthetic template spectra, representing the telluric spectrum, and a synthetic stellar photospheric spectrum to the observed spectrum of a candidate exoplanet host star in the  $2.3 \mu\text{m}$  range. This region of the K-band is rich in both deep CO  $\Delta\nu = 2$  lines for late type stars and in relatively deep lines of CH<sub>4</sub> in the Earth’s atmosphere. Precisions of

better than  $100 \text{ m s}^{-1}$  have been demonstrated by e.g., Blake et al. (2010), Figueira et al. (2010), Bean et al. (2010), Crockett et al. (2011), Bailey et al. (2012), and Davison et al. (2015) with this approach; relatively high RV precision is possible even for remarkably active T Tauri stars (Crockett et al. 2012).

For the RV standard star GJ 281, Crockett et al. (2012) used IR spectroscopy to identify an RMS scatter of  $66 \text{ m s}^{-1}$  in RV measurements taken with the CSHELL spectrograph on the NASA IRTF 3-meter over 48 epochs, and  $30 \text{ m s}^{-1}$  with the NIRSPEC spectrograph on the Keck II telescope over 9 epochs. For CI Tau, a 2 Myr old,  $0.80 \pm 0.02 M_{\odot}$  (Guilloteau et al. 2014), classical T Tauri star with an actively accreting circumstellar disk, Crockett et al. found that the amplitude of the RV variations was essentially the same in both the optical and K band, potentially suggestive of a planetary mass companion. Using the 10 optical and 14 IR measurements available at that time, Crockett et al. tentatively identified two periods in the available signals; however, no significance or uncertainty in this periodicity was identified. Since the publication of Crockett et al., we have invested considerable effort in time domain observations of CI Tau to confirm this tentative result and determine the parameters of the system. The outcome of this extended investigation is presented here. In Section 2 we describe our continued high-resolution spectroscopic observations at both optical and IR wavelengths, as well as our optical photometry. Details of our light curve and RV analyses are provided in Section 3. A discussion appears in Section 4 and we summarize our conclusions in Section 5.

## 2. Observations and Data Reduction

The observations and data reduction are described below. All the reduced data used in this paper are available for independent analysis at <http://torre.rice.edu/~cmj/CITau>.

### 2.1. IR

#### 2.1.1. IRTF

Most of our IR RVs were taken with CSHELL (Tokunaga et al. 1990; Greene et al. 1993) at the 3 m NASA IRTF. CSHELL is a long-slit echelle spectrograph ( $1.08\text{-}5.5 \mu\text{m}$ ) which utilizes a Circular Variable Filter (CVF), allowing isolation of a single order on a  $256 \times 256$  InSb detector array. For our observations, the CVF was used to allow isolation of a  $50 \text{ \AA}$  spectral window centered at  $2.298 \mu\text{m}$  (order 25). This region is favorable for

relatively precise spectroscopic analysis because of the presence of multiple photospheric absorption lines from the  $2.293 \mu\text{m}$  CO  $\nu = 2 - 0$  band head. Additionally, the presence of multiple strong telluric lines, predominantly CH<sub>4</sub> absorption features, allows us to use the Earth’s atmosphere as a “gas cell” and imprints a relatively stable wavelength reference on our observations. The 0.5” slit produced an average FWHM of 2.6 pixels ( $0.5 \text{ \AA}$ ,  $6.5 \text{ km s}^{-1}$ , measured using comparison lamp spectra), corresponding to a spectral resolving power of  $R \sim 46,000$ .

We obtained spectra of CI Tau on 34 nights between 2009 November and 2014 March (Table 1). At the beginning of each night we took 20 flat fields and dark frames along with six Ar, Kr, and Xe comparison lamp exposures to create a wavelength zero point reference and dispersion solution. All targets were observed using 10” nodded pairs which enabled subtraction of sky emission, dark current, and detector bias. Typical integration times were 600 s per nod (Crockett et al. 2011). Conditions permitting, on every night we obtained spectra of the RV standard GJ 281 and telluric standards with the identical set up except for shorter exposure times.

The data reduction strategy, implemented entirely in IDL, has been reported in our earlier publications (e.g., Crockett et al. 2012) and follows that of Johns-Krull et al. (1999). Median filtering of individual dark frames produced a master dark. A nightly normalized flat field was created by averaging the flat field exposures, subtracting the master dark frame, and then dividing by the mean of the dark-subtracted master flat. Nodded pairs of target spectra were subtracted and the difference image subsequently divided by the normalized flat field. We estimated read noise from the standard deviation of a Gaussian fit to a histogram of the pixel values in the difference image ( $\sim 30 e^-$ ). The curved spectral traces in the difference image were fit with a second-order polynomial to identify the location of maximum and minimum flux along the dispersion direction. For optimal spectral extraction, each nod pair was divided into four equally spaced bins of 64 columns along the dispersion direction. Within each of these 64 column bins we constructed a  $10\times$  oversampled “slit function” (i.e. the distribution of flux in the cross-dispersion direction). A rough estimate of the spectrum was created by summing the pixels in each column of the difference image for each nod position. The limits included in this sum are from the midpoint between the two nod positions on the detector to the edge of the area fully illuminated by the flat lamp, typically 6–70 pixels in each column for each nod position. Each pixel in the bin was then sorted by its distance from the order center for the column the given pixel falls in. The flux in each pixel was divided by the rough estimate of the spectrum for its appropriate column to normalize all the pixels going into the slit function estimate. The flux in these offset ordered pixels was then median filtered with a seven-point moving box. A flux estimate for each oversampled pixel was then determined by taking the median of all the pixels that fell

in a given subpixel. This then formed the oversampled master slit function. The multiple median filters generally remove the effects of cosmic rays and uncorrected bad pixels on the determination of the slit function. We then fit this master slit function to a three Gaussian model: a central Gaussian flanked by two satellite Gaussians. The amplitude, center, and width of each Gaussian were fit as free parameters using the IDL implementation of the AMOEBA non-linear least-squares (NLLS) fitting algorithm (Nelder & Mead 1965). The resulting model was then normalized to unit area. This algorithm produces four model slit functions, one for each bin. However, the actual slit function is a smoothly varying function of column number. Therefore, to smooth out the transitions from bin to bin, 256 column slit functions were created by linearly interpolating between the four bin slit functions.

To determine the total flux in each column of the spectrum, we calculated the scale factor that best matches the model slit function to the column data, per the recipe described in Horne (1986). In order to mask out spurious flux levels from cosmic rays, an iterative sigma-clipping algorithm was implemented. This algorithm starts with an estimate of the total noise from the measured read noise in the differenced image plus the Poisson noise from the target. We then subtracted our model fit from the data in each detector column and masked those pixels for which the residual was  $3\text{-}\sigma$  greater than the estimated noise. One or two iterations were performed until the scale factor converged, thus providing an optimal value of the spectrum in that column that is largely immune to hot pixels, cosmic rays, and other artifacts. This algorithm also provides an estimate of the flux uncertainty at each location along the spectrum.

### 2.1.2. Keck

Three IR spectra were taken with NIRSPEC on the 10-meter Keck II telescope in February and November of 2010 (Table 1). NIRSPEC is a vacuum cryogenic, high-resolution, cross-dispersed, near-IR spectrograph which operates at the Nasmyth focus. For our observations we used the N7 Filter (1.839-2.630  $\mu\text{m}$ ) with the echelle and cross-disperser angles set 62.72 and 36.24 degrees, respectively, providing imaging of orders 30 through 35 on the  $1024\times 1024$  InSb detector. The  $0.288''\times 24''$  slit yielded a median FWHM of 2.25 pixels (0.74  $\text{\AA}$ , 9.6  $\text{km s}^{-1}$ , measured from lamp spectra), corresponding to a spectral resolving power  $R \sim 31,000$ .

Multiple flat, dark, and comparison lamp frames of Ne, Ar, Xe, and Kr were taken on every night of observation. The comparison lamp lines provided an initial wavelength zero-point and dispersion solution. All targets were observed using a  $10''$  ABBA nod pattern, allowing for the subtraction of sky emission. Target integration times were typically on the

order of 30 s with 2–3 coadds. On all three nights on which we obtained CI Tau spectra we observed the RV standard GJ 281 and telluric standards; integration times were 10–20s with 2–6 coadds.

The same data reduction procedure was applied as for the CSHELL observations (§2.2.1) except that a fourth-order polynomial was used to trace the location of the spectra on the detector instead of a second-order polynomial. Reductions were limited to spectral order 33 (2.286–2.320  $\mu\text{m}$ ) because it contains the requisite stellar CO and telluric CH<sub>4</sub> lines and encompasses the CSHELL bandpass which allows for more direct comparison of the two instruments.

### 2.1.3. KPNO

Observations of CI Tau and GJ 281 were obtained with the Phoenix IR echelle spectrometer (Hinkle et al. 1998) during four separate observing runs in 2013 and 2014. Data were obtained at the KPNO 4 m Mayall telescope from 27 February 2013 through 3 March 2013. All other KPNO data were obtained at the 2.1 m telescope between 9 November 2013 and 10 January 2014 (Table 1). At both telescopes the four-pixel slit was used, corresponding to  $0.''7 \times 28''$  at the Mayall 4 m and  $1.''4 \times 56''$  at the KPNO 2.1 m. The grating was configured to provide wavelength coverage from 2.2943 – 2.3040  $\mu\text{m}$ , and the K4308-order blocking filter was used to eliminate light from any overlapping orders. This setup yielded a spectral resolution of  $R \sim 50,000$  at both telescopes. Observations of each star were taken in pairs with a nod of  $10''$  along the slit for the Mayall 4 m telescope and a nod of  $20''$  along the slit at the KPNO 2.1 m telescope. Signal-to-noise ratios (SNR) varied significantly for the Phoenix observations depending on the combination of object brightness, telescope used, and observing conditions for the observation. At the Mayall 4 m, typical observations on CI Tau consisted of four 600 s exposures, while for GJ 281 two 600 s exposures were most often used. At the KPNO 2.1 m, eight 900 s observations were typically made of CI Tau, while four 900 s exposures of GJ 281 were sufficient. A total of 19 observations of CI Tau and 9 of GJ 281 were taken. In addition to stellar spectra, flat field and dark exposures were also obtained, as well as exposures of a ThArNe lamp in order to provide wavelength calibrations. All of the data were reduced using custom IDL routines. These are essentially the same routines used to reduce the CSHELL data, with small modifications made to account for the differences in detector size and data formats of each instrument.



#### 2.1.4. *McDonald Observatory*

We obtained 14 observations of CI Tau on the Harlan J. Smith 2.7-meter telescope with the Immersion GRating INfrared Spectrograph (IGRINS) in 2014 November and December and 2015 January (Table 1). IGRINS implements silicon immersion gratings, a fixed optical path (no cryogenic mechanisms), and volume-phase holographic gratings to simultaneously cover the H and K bands (1.48-2.48 $\mu$ m) with a resolving power  $R \sim 45,000$ . The echellogram for each band is projected onto a pair of 2048 $\times$ 2048 pixel Teledyne H2RG HgCdTe detectors. IGRINS straightforward design and high throughput make observations on the 2.7 m Harlan J. Smith Telescope at McDonald Observatory comparable to spectrographs at 8 m facilities, but with 5 times to 100 times the spectral grasp. Additional discussion on the design and capabilities of IGRINS appears in Park et al. (2014).

Observations with IGRINS employed standard near-IR techniques. CI Tau was nodded between two positions, separated by 7"0, along the 1 $\times$ 15 arcsecond slit. The IGRINS pipeline package PLP<sup>1</sup> was developed by Dr. Jae-Joon Lee at Korea Astronomy and Space Science Institute and Professor Soojong Pak's team at Kyung Hee University. The pipeline subtracts AB pairs to remove OH emission lines and then optimally extracts the sources based on the methods of Horne (1986). The wavelength solution is determined first from ThAr lamp spectra taken at the start of each night, and then improved by fitting the OH lines in the two dimensional target spectra. The flux, wavelength, signal-to-noise and variance of every extracted order is output as a FITS file for the H and K bands separately. For our determination of CI Tau RVs we employed the CO bandhead lines redward of  $\sim 2.295 \mu$ m.

## 2.2. Optical

### 2.2.1. *Echelle Spectroscopy*

CI Tau was included among the earliest subset of targets observed in our McDonald Observatory RV survey of  $\sim 140$  stars in the Taurus region to look for evidence of young, very low-mass companions to newly formed stars. The observational setup has been described in previous papers from this work (Huerta et al. 2008; Prato et al. 2008; Mahmud et al. 2011; Crockett et al. 2012); we provide a brief summary here. Spectra were obtained with the Robert G. Tull Coudé Spectrograph (Tull et al. 1995) at the McDonald Observatory 2.7 m Harlan J. Smith telescope. A total of 29 spectra were obtained between 2004 December

---

<sup>1</sup>Currently available at: <https://github.com/igrins/plp>

28 and 2013 November 15 (Table 2). A 1."2 slit yielded a spectral resolving power of  $R \equiv \lambda/\Delta\lambda \sim 60,000$  for spectra covering the wavelength range 3,900 – 10,000 Å with small wavelength gaps between the redder orders starting at  $\sim 5,600$  Å. Integration times varied from 1200 s to 3000 s, depending on conditions, but were usually 2400 s. The average seeing was  $\sim 2''$ . We took ThAr lamp exposures before and after each spectrum for wavelength calibration; typical rms values for the dispersion solution precision were  $\sim 4 \text{ m s}^{-1}$ .

The optical echelle spectra were reduced using a suite of IDL routines that have been described in various references (e.g., Valenti 1994; Hinkle et al. 2000). These routines form the basis of the REDUCE IDL echelle reduction package (Piskunov & Valenti 2002). The raw spectra were bias-subtracted using the overscan region and flat-fielded using the spectrum of an internal continuum lamp. Optimal extraction to remove cosmic rays and improve signal was used for all the spectra. The wavelength solution was determined by fitting a two-dimensional polynomial to  $n\lambda$  as function of pixel and order number,  $n$ , for approximately 1800 extracted thorium lines observed from the internal lamp assembly. The final wavelength solution used for each observation was the average of solutions from ThAr lamp exposures taken before and after each stellar exposure.

### 2.2.2. Photometry

The photometry was obtained with the Lowell 0.7 m f/8 reflector in robotic mode. It has a permanently mounted CCD camera that provides a  $15' \times 15'$  field at an image scale of  $0''.9 \text{ pixel}^{-1}$ . The CI Tau field was targeted on fourteen nights between 2012 November 7 and December 11 UT. We obtained two 3-minute exposures in the V filter at each visit, with several visits each night yielding 189 data points (Table 3). The images were reduced via ordinary aperture photometry with the commercial photometry package *Canopus* (version 10.4.0.6). The four comparison stars were found to be constant over the observation interval. V magnitudes for these standard stars were adopted from ASAS-3 (Pojmanski 1997) and APASS (Henden & Munari 2014) to adjust the data approximately to standard V magnitudes. Because of the emission-line nature of the CI Tau spectrum, there will inevitably be a small zero-point shift dependent on the color of the comparison stars and the passband of the filter + CCD system. Our mean magnitude near V=13.0 is nevertheless similar to the longer-term ASAS-3 value (V=13.04), the TASS MkIV series (V=13.1; Droege et al. 2006), and APASS with sparser observations (V=12.94).

### 3. Analysis

#### 3.1. IR RVs

All near-IR K-band observations were processed in essentially the same way using procedures described by Crockett et al. (2011). The RVs were determined using a spectral modeling technique in which template spectra for the stellar spectrum and the telluric spectrum are combined to model each of the observed spectra of CI Tau. We interpolated over a grid of NextGen models (Hauschildt et al. 1999) to produce a synthetic stellar atmosphere tailored to the  $T_{eff}$ ,  $\log g$ , and metallicity assumed for CI Tau. We then used SYNTHMAG (Piskunov 1999) to create a template stellar spectrum with this model atmosphere using an atomic line list from Kupka et al. (2000) and a CO line list from Goorvitch (1994). For the telluric spectral template, we used the NOAO telluric absorption spectrum of Livingston & Wallace (1991). The telluric absorption features in the K band provide an absolute wavelength and instrumental profile reference, similar in concept to the iodine gas cell technique used in high-precision optical RV exoplanet surveys (Butler et al. 1996).

We fit our observed spectra with the templates by fitting a number of free parameters including a velocity shift and a power-law scaling factor for both the stellar and telluric template. The stellar rotational and instrumental broadening are also free parameters, as is a second-order continuum normalization, and a second-order wavelength dispersion. The model spectrum is fit to each observed spectrum using the Levenberg-Marquardt method (Bevington & Robinson 1992) to optimize the parameters of the model. The wavelength shift of the stellar template relative to the telluric template is then the measured RV of the star, which we then correct for the motion of the barycenter. We used a Monte Carlo technique to estimate the errors in the model parameters. For each observation, we generated 100 simulated observations based on the measured noise in the spectrum and refit the model to each of the simulated observations. The standard deviation of the 100 results for each parameter, and in particular the RV, was taken as the statistical uncertainty for that observation.

For the case of the Phoenix and IGRINS spectra where only the one final observed spectrum for each night is produced by the reduction (see §2.2.3 and §2.2.4), the above procedure gives the final RV and associated uncertainty. In the case of CSHELL and NIRSPEC data, we perform the above RV analysis on each nod position in each exposure separately. The final, nightly RV was then determined by calculating the average of the individual nod RVs, weighted by their uncertainties. The final uncertainty in the nightly RV was computed by taking the weighted standard deviation of the nod RVs and dividing by the square root of the number of nods.

The above procedure gives only an estimate of the statistical uncertainty in each RV measurement based on the signal-to-noise in each spectrum. We have previously assessed the long-term systematic uncertainties in our observations by routinely observing stars known to have stable RVs (i.e.  $< 50 \text{ m s}^{-1}$ ; Prato et al. 2008; Mahmud et al. 2011; Crockett et al. 2012). For CSHELL we have determined that the long term stability in this technique is  $66 \text{ m s}^{-1}$  and for NIRSPEC we have determined this long term uncertainty to be  $30 \text{ m s}^{-1}$  (Crockett et al. 2012). In the case of Phoenix, we have a total of 9 observations of our RV standard GJ 281, and the standard deviation of our RV measurements for this star is  $62 \text{ m s}^{-1}$  which we take as the systematic uncertainty for our Phoenix observations. This value is very similar to, but slightly better than what we get for CSHELL. The slight improvement may be the result of the fact that Phoenix has a somewhat higher resolution and about twice the wavelength coverage of CSHELL. We have only 4 observations of GJ 281 with IGRINS, which is similar in resolution to CSHELL but covers a wider wavelength range in the region of interest. The standard deviation of these observations is  $52 \text{ m s}^{-1}$ ; however, given the small number of observations, we assign a more conservative systematic uncertainty to our IGRINS measurements of  $75 \text{ m s}^{-1}$ . We then add these systematic uncertainties in quadrature with the statistical uncertainty from each night’s observation to obtain a final RV uncertainty for each observation. Our measured RVs and uncertainties for CI Tau for each IR spectrograph are presented in Table 1.

All of our K band RV measurements were calculated with respect to the same reference: the telluric spectrum. Therefore, we combine the measurements from all instruments together and analyze them as one group with no zero point adjustments. For the plots and the values in Table 1, we have subtracted the mean of all the IR RV measurements from the reported values. We then used the Lomb-Scargle periodogram technique (Horne & Baliunas 1986) to search for periodicity in the IR RV measurements. Given the relatively large RV uncertainties we obtain, our data are primarily sensitive to Jupiter mass or larger companions in relatively tight orbits. Therefore, our initial periodogram search was in the range of 2 – 20 days (the lower bound on the period set by the Nyquist frequency since our observations are usually taken 1 day apart or longer). The power spectrum is shown in Figure 1, where a strong peak is apparent at 8.99 days. We also searched the periodogram between 20 – 100 days for completeness; however, no strong peaks appear in this range (the periodogram peak in this range has a value of 5.8 with a false alarm probability of 0.22). We estimated the false alarm probability in the power spectrum peak of Figure 1 using a bootstrap method where we randomly reordered our RV measurements to create new data sets observed with the same temporal sampling as our observations, ensuring a consistent variance for each data set. We then computed the power spectrum of each data set over the same 2 – 20 day period range as done for the original data and repeated this process 10,000 times. In doing so, we

found that the false alarm probability for the peak seen at 8.99 d in the IR data is  $6 \times 10^{-4}$ . When we fit the RV data with a Keplerian orbit (below) and subtract this fit from the data, the 8.99 d peak and the nearby peak at  $\sim 9.2$  d vanish from the power spectrum, indicating that there is only one potentially periodic signal present near this period.

Interpreting the periodic RV variation seen in the IR spectra of CI Tau as orbital motion resulting from a low mass companion, we performed a Keplerian fit to the velocity variations. In the orbit fitting, we keep as fixed the orbital period as determined from the power spectrum analysis and treat as free parameters the center-of-mass velocity of the system, the eccentricity, the velocity amplitude for CI Tau, the longitude of periastron, and the phase of periastron passage. We use the nonlinear least-squares technique of Marquardt (Bevington & Robinson 1992) to find the best-fit parameters for the orbit (Table 4, column for IR only fit). While we used the peak in the power spectrum as our initial guess for the period, we determined the more accurate period, reported in Table 4, that gives a  $\chi^2$  minimum for the orbital fit by densely sampling periods near the periodogram peak period and fitting a parabola to the resulting  $\chi^2$  values. The observed IR RVs for CI Tau, phased to this 8.9965 day period, along with the orbital fit are shown in Figure 2; there is considerable scatter around the fit (RMS of  $0.694 \text{ km s}^{-1}$ ) which we believe is astrophysical in origin. We discuss the potential causes of this in §4. Uncertainties in the orbital fit parameters are derived by Monte Carlo simulation of the data: for 1000 simulations we construct fake RV data using the RV fit and applying Gaussian random noise with a standard deviation equal to that in the residuals from the fit of Figure 2. We then analyze these model data using the same procedure outlined above for the actual observations. In doing so, we keep the data uncertainties equal to the values reported in Table 1 for the purpose of the orbit fitting. The resulting uncertainties in the orbital parameters, reported as the standard deviation of the derived properties, appear in Table 4, and the distributions of the derived periods, eccentricities, and  $M_p \sin i$  values are shown in Figure 3. The inclination dependent planetary mass of  $8.81 \pm 1.71 M_{Jup}$  was derived assuming a stellar mass of  $0.80 \pm 0.02 M_\odot$  for CI Tau (Guilloteau et al. 2014). The uncertainty of the planet’s mass incorporates this uncertainty in the stellar mass. Guilloteau et al. determined a circumstellar disk inclination for CI Tau of  $45.7 \pm 1.1^\circ$ ; assuming that the planet and the disk are coplanar, we find an absolute mass for CI Tau b of  $12.31 \pm 2.39 M_{Jup}$ .

### 3.2. Optical RVs

We followed the approach of Huerta et al. (2008) and Mahmud et al. (2011) and determined optical RVs using a cross-correlation analysis of nine orders in the echelle spectra.

Each order contains  $\sim 100 \text{ \AA}$ , and the nine orders span the wavelength range  $5,600\text{--}6,700 \text{ \AA}$ . Orders were chosen for analysis based on high signal-to-noise ratio, a lack of stellar emission lines, and a lack of strong telluric absorption lines present in the order. We used the mean of the RV measurements from the multiple echelle orders as the final RV value, while the standard deviation of the mean is assumed to be the internal statistical uncertainty in the RV measurement. We used the CI Tau observation with the highest signal-to-noise ratio (JD 2455160.819) as the template for the cross-correlation analysis. Three of the observed optical echelle spectra were not suitable for RV determinations owing either contamination by a weak solar spectrum due to observations made through moderate cloud relatively close to the Moon, or to relatively low signal-to-noise ratios in the continuum and/or large veiling values which resulted in weak photospheric lines and very large RV uncertainties; however, these observations remain useful for the emission line analysis. The RVs for these data are not reported in Table 2. The measured velocities were then corrected for the motion of the barycenter and the mean RV of the optical measurements was subtracted from all the values as we are only interested in relative velocity variations in this study. These final optical RV measurements are presented in Table 2. As discussed in previous studies from this series (e.g., Huerta et al. 2008; Prato et al. 2008; Mahmud et al. 2011; Crockett et al. 2012), we have observed several RV standards known to be stable at a level of a few  $\text{m s}^{-1}$  to assess the long term stability of our measurement technique. We find that our observations of these stars show an RV standard deviation of  $\sim 140 \text{ m s}^{-1}$  for optical wavelengths, which we take as the intrinsic uncertainty in our method. We add this in quadrature to the internal uncertainties determined above to get a final optical RV measurement uncertainty, also reported in Table 2.

In §4 we discuss the possibility that the RV variations recorded for CI Tau result from an accretion hot spot. This hypothesis can potentially be tested by examining the variations in the veiling on CI Tau, and by examining the behavior of the narrow component (NC) of emission lines such as He I  $5876 \text{ \AA}$  and the Ca II IR triplet (IRT). Veiling in CTTSs is the apparent filling in or weakening of photospheric absorption lines caused by a featureless continuum, believed to result from the shock which forms when accreting disk material impacts the stellar surface (e.g., Hartigan et al. 1989). In this study we are only interested in the variations in the veiling, so we measure a veiling,  $r$ , relative to the observation of CI Tau with the strongest absorption lines. An accurate measure of veiling on spectra with moderate signal-to-noise such as these is aided by combining information from as many lines as possible. One such method of doing this is to use the least squares deconvolution (LSD) technique introduced by Donati et al. (1997). This technique assumes the observed spectrum is the convolution of a single intrinsic photospheric line profile convolved with a series of delta functions whose location and amplitude give the wavelength and intrinsic depth of each line

in the spectrum. Using a constant line list, the LSD technique can be used to deconvolve the spectrum to obtain the intrinsic photospheric profile of each observation. If the lines in a given spectrum all get weaker because of an increase in veiling, the recovered intrinsic profile will also get weaker. As a result, we can compare the recovered LSD profiles from each observation and measure a very accurate relative veiling using the observation with the strongest LSD profile as the reference spectrum. For the measurements here, we used the LSD code of Chen & Johns–Krull (2013) and a custom line list made using the VALD database (Kupka et al. 2000). The final line list contains a total of 1944 lines spanning the wavelength range 5350 – 8940 Å. The majority of the lines are found in the 5350 – 6500 Å range. We used the observation from JD 2456605.906 as the reference spectrum, with veiling  $r = 0.0$  by definition; all other values of veiling reported in Table 2 are relative to this observation.

The He I 5876 Å and Ca II emission lines of many CTTSs appear to be made up of a narrow component (NC) sitting on top of a broad component (BC) of the line (e.g. Batalha et al. 1996; Beristain et al. 2001; Alencar & Basri 2000). Here, we are interested in the radial velocity of the NC of the line. In order to isolate just this component, we follow the example of several earlier investigators (Johns & Basri 1995; Alencar & Basri 2000; Sicilia–Aguilar 2015) and fit each observed emission line with multiple Gaussians. In our spectra, the only IRT line present is the 8662 Å line so we fit this and the He I line. Given the higher signal-to-noise ratio and complexity of the former, we required four Gaussian components to properly fit the Ca II line while we needed just two Gaussian components to fit the He I line. For each spectrum we averaged the wavelength solution from the Th-Ar lamp spectra taken immediately before and after each stellar spectrum. The wavelength of the NC fit was then translated into an RV and the motion of the barycenter was removed. We estimate the uncertainty in the RV by performing a Monte Carlo analysis on the fit, adding in normally distributed random noise at a level given by the signal-to-noise in each observation for the line in question. A total of 100 Monte Carlo trials were performed for each line fit and the standard deviation of the resulting RV values was taken as the uncertainty. To this, we added in quadrature the  $140 \text{ m s}^{-1}$  systematic uncertainty identified above for the photospheric RV analysis. The NC RV and its uncertainty for both the He I 5876 Å and Ca II 8662 Å lines are reported in Table 2.

CI Tau was identified as a potential host of a several Jupiter mass planetary companion by Crockett et al. (2012) because of its significant optical RV variations and IR (K band) RV variations of similar amplitude; however, these results were based on a relatively small number of data points (10 optical and 14 IR). We now have 26 optical RV data points. We computed a power spectrum of the optical RV measurements, again using the Lomb-Scargle periodogram technique (Horne & Baliunas 1986). The strongest peak in the power spectrum

occurred at a period of  $\sim 9.5$  d with a false alarm probability (determined from a Monte Carlo analysis) of 0.017. The second strongest peak in the power spectrum is nearly as strong and occurred at a period of  $\sim 7.2$  d, also with a false alarm probability of 0.017. These peaks are suggestive, particularly since the 7.2 d period is very close to the period found below for the variability of the optical photometry (§3.3), and the 9.5 d period is close to the 8.99 d period found for the variability of the IR RV measurements above (§3.1). However, to independently confirm *periodicity*, it is generally desirable to have a false alarm probability that is lower than the 0.017 observed in the optical data. As a result, the optical data alone do not represent as significant a detection of a periodic signal as the IR data.

### 3.3. Combined IR and Optical RVs

Given the periodic signals suggestive of a giant exoplanet with a period of  $\sim 9$  d (IR) to  $\sim 9.5$  d (optical), we combined the optical and IR mean subtracted RV data into one time series for analysis. We again used the Lomb-Scargle periodogram technique to compute the power spectrum of this combined data set (Figure 4). The peak near 9 days has become even stronger, but has shifted slightly to 8.9965 d instead of 8.9891 d; however, this is well within the period uncertainty determined from the analysis of the IR RV data alone (Table 4). We again use a bootstrap Monte Carlo technique to estimate the false alarm probability for this peak, this time utilizing  $10^6$  trials sampling the period range 2 to 20 days as done initially for the analysis of the real data. From this simulation, we estimate a false alarm probability of  $8 \times 10^{-6}$ . We also performed a periodogram analysis of the data in the range 2 to 100 days and find that the 8.99 day period remains the strongest peak in the data. The Monte Carlo simulation sampling the same 2 to 100 day period range to estimate the false alarm probability again yields a value of  $8 \times 10^{-6}$ .

We follow the same procedure described above to fit a Keplerian orbit to this combined dataset and to estimate the uncertainties in the orbital parameters. The RV fit is shown in the bottom panel of Figure 4, which is almost identical to Figure 2. This suggests that the optical data do show evidence for the planetary companion, but that activity-induced RV noise muddies the planet’s signal in the optical data to some degree. The RMS of the fit residuals to the combined IR+optical RVs is slightly greater at  $0.728 \text{ km s}^{-1}$  than for the IR data alone, again likely the result of the increased activity related noise in the optical RV measurements. The orbital parameters and associated uncertainties are given in Table 4 and the distribution of the derived periods, eccentricities, and  $M_P \sin i$  are shown in Figure 5. We have subtracted this RV fit from the RV data points and recomputed the power spectrum of the residuals. The highest peak in the power spectrum occurs at a period of 4.75 d and has



a false alarm probability of 0.07. As an additional test to see how strongly the optical data might be affected by (and potentially biased by) spot-induced RV noise, we subtracted the IR only RV fit (Figure 2) from the optical RV data and computed the power spectrum of those residuals. Again, no significant peaks were found: the strongest occurs at  $\sim 4.6$  d with a false alarm probability of 0.146. This could indicate that the activity-induced variations of CI Tau do not remain coherent over the  $\sim 9$  year span of this data, the result perhaps of the migration of spots (e.g., Llama et al. 2012) or their disappearance from one region of the stellar surface and reemergence in another over the years of observation. Because CI Tau is a CTTS, there are many potential sources of variation in addition to dark, cool spots.

The IR data alone phase nearly as well to the 8.9891 d period, found for the combined IR plus optical data set (Figure 4), as it does to the 8.9965 d IR only period (Figure 2). The optical data in the bottom panel of Figure 4 phases fairly well to this period, although there are a few significant outliers that may represent times when spot induced noise was particularly problematic. We emphasize that the amplitude of the optical RV variations is the same as that of the IR RV variations to within their uncertainties. If we hold the orbital period and eccentricity fixed to the values found from the combined fit and fit only the IR RV data points we find a velocity amplitude of  $K = 0.99 \pm 0.17$  km s $^{-1}$ . If we then fit only the optical RV points holding the period and eccentricity fixed to the same values, we find  $K = 0.63 \pm 0.23$  km s $^{-1}$  (the lower significance of this fit is a combination of the fewer number of optical observations and the additional scatter present in the optical RVs, which in turn prevented a definite detection of this signal in the optical-only periodogram analysis described above). Thus, the optical amplitude is found to be lower than that in the IR, but the difference is not statistically significant.

The ratio of the optical to IR RV amplitudes is  $0.64 \pm 0.26$ . If cool, dark spots were responsible for the RV signals in both the optical and IR, we would expect this ratio of the optical to IR RV amplitudes to be  $>4$  because spot noise has a higher impact on the optical RVs (Mahmud et al. 2011). From the combined dataset, the candidate planet’s mass is  $M_P \sin i = 8.08 \pm 1.53$  M $_{Jup}$ . Again assuming a stellar mass of  $0.80 \pm 0.02$  M $_{\odot}$  for CI Tau (Guilloteau et al. 2014), and using an inclination of  $45.7 \pm 1.1^\circ$  for CI Tau b based on the inclination of the circumstellar disk (Guilloteau et al.), we get an absolute mass for CI Tau b of  $11.29 \pm 2.13$  M $_{Jup}$ . These values are very similar to those determined using the IR RV measurements alone.

The eccentricity we find for CI Tau with the combined IR and optical orbital solution,  $0.28 \pm 0.16$ , is relatively large compared with typical eccentricities of hot Jupiters orbiting mature stars, which are usually  $<0.1$  (Fabrycky & Tremaine 2007). However, the eccentricity of a few Myr old object is likely to be a property which either evolves toward zero as the result

of dynamical interactions with disk material and/or other planets, or could potentially be a property which dooms a massive planet to orbital decay and consumption by its parent star. Alternatively, high-eccentricity giant planets may be dynamically ejected from their host system. Anecdotally, with the accumulation of larger data sets, hot exo-Jupiter eccentricity estimates tend to decrease. Thus as we collect more data we will examine the cumulative changes, if any, in eccentricity and other orbital parameters.

### 3.4. Optical Light Curve

We used both a Fourier-fitting routine (Harris et al. 1989) and the Lomb-Scargle method (Horne & Baliunas 1986) to look for photometric periodicity. Both approaches yielded significant power at a period of  $\sim 7.1$  days. The latter technique gives a false-alarm probability of  $< 10^{-4}$ . This value was again obtained by running 10,000 Monte Carlo simulations of the data, sampling the observed photometry randomly over the epochs of observation. Figure 6 displays the Lomb-Scargle power spectrum. While the power in the periodogram is quite strong, and the data clearly show systematic variations, the periodogram only samples this potential period in a limited way. The photometric data were taken in 3 runs spanning a total of 34 days. Figure 7 shows the photometry with each observing run color coded. The top panel shows the data phased to the 7.1 d period found in the periodogram analysis. The bottom panel shows the data phased to the 8.99 d period found in the RV analysis (the figure looks the same whether we phase to 8.997 d or 8.994 d as these two periods are so close and the length of the photometric campaign was so short that there is a maximum phase shift of only 0.002 between the two periods). Clearly the data are not strictly periodic in either panel, though in the top panel (7.1 d) the data from all 3 runs show a decline in brightness at approximately the same phase. For the two runs that cover the latter phases, the brightness recovers fully at about the same phase as well, but one of these runs shows a substantially deeper minimum. Whatever is causing the decline in brightness changed measurably from one phase to the next, or possibly other factors contributed to augment the dimming. The bottom panel, phased to 8.99 d, shows no clear behavior from one phase to the next. Because of the intrinsic jitter in the variability of this system, we are not able to determine a definite photometric period for CI Tau; however, the data do not support a period near 9 days, and instead point to a period closer to 7 days for this star.

### 3.5. H $\alpha$ Analysis

All 29 optical echelle spectra of CI Tau show strong, variable H $\alpha$  emission. Figure 8 shows the average H $\alpha$  profile of CI Tau plotted in the stellar rest frame. This average profile has an emission equivalent width of 69.6 Å. We computed the power spectra, again using the Lomb-Scargle method (Horne & Baliunas 1986), of the relative flux variations in each 5 km s<sup>-1</sup> velocity channel across the H $\alpha$  emission line. We found that the velocity channel at  $\sim 200$  km s<sup>-1</sup> (Figure 9a) shows the strongest power, 11.0, in the periodogram analysis; this peak occurs at a period of 9.4 days. The next two strongest peaks in this channel appear at periods of 9.0 and 9.2 days. The surrounding nine independent velocity channels, between 181 and 227 km s<sup>-1</sup>, also show a power spectrum peak in their relative H $\alpha$  flux variations at 9.4 days. Figures 9b and 9c illustrate the power spectrum from two other velocity channels in the H $\alpha$  line. Figure 9b shows the power spectrum of the 0 velocity channel, while Figure 9c shows the velocity channel at  $-135$  km s<sup>-1</sup> which is the channel that shows the strongest fractional variation in the profile. This blue-shifted velocity channel is near the center of a variable absorption component that sometimes appears the profile, indicative of a variable wind flowing from CI Tau. These additional power spectra indicate the “typical” strength of the periodograms outside the strongest one at  $\sim 200$  km s<sup>-1</sup>. The flux variations for the the 200 km s<sup>-1</sup>, phased to a 9.4 day period, are shown in Figure 10a. Again using a Monte Carlo analysis to resample the observed flux values in a random order while preserving the actual dates of observation, we found that the 9.4 day period peak in the 200 km s<sup>-1</sup> velocity channel has a false alarm probability less than  $10^{-4}$  and any peak stronger than 9.8 has a false alarm probability of  $10^{-3}$  or less.

While the phased flux curve in Figure 10a shows little scatter, the power spectrum in Figure 9a shows strong power at many periods, making it unclear whether there is a true period present. If we fit the phased flux curve in Figure 10a with a sine wave and subtract the fit from the data, we can compute the power spectrum of the residuals. Doing so gives a periodogram with a peak of only 6.3 at a period of  $\sim 2.3$  d, near the theoretical Nyquist limit for data sampled 1 day apart as is typically the case for the individual runs on which these observations were obtained. The false alarm probability for a peak this strong is 0.254. For periods longer than 3 d, the peak in the residual power spectrum occurs at  $\sim 14.7$  d with a power level of 5.5, corresponding to a false alarm probability of 0.499. While the peak in the power spectrum of the flux variations occurs at  $\sim 9.4$  d, the next two peaks are very close in strength and produce phased variability with little scatter. For example, phasing to the peak at  $\sim 9.0$  d produces the curve shown in Figure 10b. Thus we conclude that if there is periodic modulation in the H $\alpha$  line of CI Tau, there is only one significant period in the 9.0 – 9.4 d range. These peak periods are suggestively close to the same period as found in the IR RV variations, possibly indicating that the source of the RV variations is also influencing

the behavior of the H $\alpha$  line.

## 4. Discussion

### 4.1. The Role of Accretion Hot Spots

Dark, cool spots can produce RV signals on a rotating star that mimic those from a low mass companion (e.g., Saar & Donahue 1997; Desort et al. 2007; Reiners et al. 2010). To first order, this results because the dark spot removes a contribution to the photospheric absorption lines at the projected RV of the region of the rotating star where the spot is found. This leads to a distortion in the line profile which can appear as a small RV shift. In the case of dark spots, their presence can be diagnosed on the basis of the wavelength dependence of their effect; spots are not completely dark, and become much less so at IR wavelengths relative to the optical (e.g., Martin et al. 2006; Huelamo et al. 2008; Prato et al. 2008; Mahmud et al. 2011). This fact, and the observation that the RV amplitude of CI Tau is nearly identical in the optical and the IR, suggests that dark cool spots are not the cause of the observed RV signal in this star; however, there remains the possibility of hot spots.

Bright accretion spots on classical T Tauri stars can in principle create the same apparent RV signal as dark spots (e.g., Kóspál et al. 2014; Sicilia-Aguilar et al. 2015). Accretion hot spots which produce veiling on CTTSs typically have temperatures  $\sim 10,000$  K and produce a largely featureless continuum (Hartigan et al. 1989; Basri & Batalha 1990; Hartigan et al. 1991; Valenti et al. 1993). As a result, these hot spots do not contribute to the cool ( $\sim 4,000$  K) photospheric absorption lines at the projected RV of the spot and distort the line profile shape in the same way that a dark, cool spot would. Furthermore, because these spots are hotter than the stellar photosphere, it is expected that they produce essentially identical line profile distortions (and hence apparent RV signals) in the optical and the IR. Thus, we can not use the similarity of amplitude in the optical and IR RV signals to rule out bright accretion spots as the source of the observed RV signals in CI Tau. However, if bright accretion spots are responsible for the observed RV signals, various simple predictions may be explored to test this hypothesis. These include photometric variability produced by the accretion spots, potential correlation between the veiling and the measured RV signals, and anti-correlation between the RV of lines formed in the hot spot with the photospheric RV signals. We consider each of these in turn.

The IR RV measurements presented here were taken over a time span of  $\sim 5$  years. Including all the optical data, the time span over which all the RV measurements we obtained

is  $\sim 10$  years. The RV measurements appear to be well phased over the 5 years in which the IR observations were made (Figure 2), and with a small modification to the period (well within the period uncertainty), the full dataset shows good coherence over 10 years (Figure 4). In order for a hot spot to produce such a RV signal, it too would have to be coherent over a similarly long time span, and thus might be expected to show rotationally modulated photometric behavior. Our own photometry presented above does show apparent modulation; however, while not well-determined, the period is not consistent with the 8.99 d period found in the RV signals (Figure 7). In addition to our own observations of CI Tau, others have monitored this star photometrically. Grankin et al. (2007) observed CI Tau photometrically a total of 320 times between 1987 and 2003. Artemenko et al. (2012) report a period of 16.10 days based on this data. We have downloaded this photometric database and performed periodogram analyses on the entire dataset and on each observing season subset of the data. The highest peak we recover in the power spectrum of the entire dataset is at a period of 16.24 days with a false alarm probability of 4.6%. We assume this is the same signal Artemenko et al. report at a period of 16.10 days. We do not consider this a firm detection. Analyzing each observing season individually does not reveal stronger periodicity, and in no case do we find significant periodicity near 9 days. Percy et al. (2010) used a “self-correlation” analysis on this same photometric data, augmented by a few (12) additional observations and report a period of 14.0 days for CI Tau. While the photometric period for CI Tau remains uncertain, the existing photometry does not suggest a period of 9 days for this star.

In addition to producing a photometric signal on CI Tau, if a hot spot is the cause of the observed RV variations, it is possible that there will be a relationship between the observed RV signals of CI Tau and the veiling. When the hot spot is most directly facing the observer (effectively in the middle of the star), the veiling should be largest and the RV should not be affected. As the spot moves to either limb, the veiling should decrease and the RV will become either red- or blue-shifted depending on which limb the spot is on. Thus, a plot of veiling versus photospheric RV might show a parabolic relationship with the veiling largest at 0 relative velocity. For our optical data, the observed relationship between veiling and photospheric RV is shown in the bottom panel of Figure 11; no correlation was observed. We performed a correlation analysis (both linear correlation and Spearman’s and Kendal’s  $\tau$  rank order correlation) on the veiling and optical photospheric RV measurements and found no relationship at all between the two quantities.

The above predictions relating photometric brightness or veiling to the photospheric RV caused by a hot spot implicitly assume that when the accretion related continuum emission changes intensity, the property of the hot spot that is primarily varying is its projected area. If on the other hand, accretion variability causes the surface flux from the hot spot to

change substantially on short timescales, it may be difficult to detect rotationally modulated signals from the hot spot related continuum emission. Spectroscopic studies of the veiling continuum emission (e.g. Valenti et al. 1993; Gullbring et al. 1998; Cauley et al. 2012) find that the accretion continuum is produced in marginally optically thick gas. These studies also find that the temperature of the gas producing the hot spots are all close  $\sim 10,000$  K. This suggests that the surface flux of the accretion hot spots is very similar from star to star. Using the parameters of the accretion emission published by Cauley et al. (2012), we find that the accretion luminosity is very well correlated with the area of the star covered by the accretion spots. The studies above compare the properties of accretion spots from one CTTS to another; however, simulations of variable accretion onto individual CTTSs show that variations in the area of the accretion spots are highly correlated with the instantaneous accretion rate (e.g. Romanova et al. 2008; Kulkarni & Romanova 2008; Kurosawa & Romanova 2013). Indeed, Batalha et al. (2002) performed a variability study of the CTTS TW Hya and find that the projected area of the hot spot is well correlated with the hot spot luminosity and resulting veiling. Therefore, we suggest that the hot spot emission strength on CI Tau may be a good diagnostic of the projected area of the hot spot on this star as assumed in the tests described above.

Another prediction of the accretion hot spot on a rotating star hypothesis is that there should be apparent rotational modulation of emission lines formed in the accretion footprints themselves. Further, because these emission lines reveal the actual motion of the hot spot, whereas the impact of the hot spot on the photospheric absorption lines is to remove a contribution to the line profile, the modulation of the hot spot emission lines should be  $180^\circ$  out of phase with the photospheric lines. Thus, plotting the emission line RV versus the photospheric RV should show an inverse correlation. Such behavior has been seen in the star EX Lup by Kóspál et al. (2014) and has been modeled as an accretion spot by Sicilia-Aguilar et al. (2015). The lines showing this behavior are the narrow components (NCs) of metallic emission lines such as that from He I 5876 Å and the Ca II IR triplet. It has long been expected that the NCs of these and other emission lines form in the post-shock region (e.g. Batalha et al. 1996; Beristain et al. 2001) at the base of the accretion footprints. As a result, the NC of these emission lines serve as a good indicator of the behavior and location of accretion footprints, and they have even been used to Doppler image the location of accretion footprints on CTTSs (e.g., Donati et al. 2008, 2010).

We have estimated the location and size of the hot spot required to produce the observed photospheric RV modulation using the disk integration code utilized by Chen & Johns-Krull (2013). A single hot spot is assumed on the surface of CI Tau, and we assume a stellar inclination of  $45.7^\circ$  (Guilloteau et al. 2014) and a  $v \sin i = 11 \text{ km s}^{-1}$  (Basri & Batalha 1990). We find a best fit to the observed photospheric RV measurements for a hot spot located

at a latitude of  $82^\circ$  covering a maximum projected area 46.7% on the surface of the star. Such a large areal hot spot coverage is far greater than values typically found on CTTSs which are usually in the few percent range (e.g., Valenti et al. 1993; Calvet & Gullbring 1998). However, there is a degeneracy between the spot latitude and the size such that a hot spot covering only 10% of the stellar surface at a latitude of  $16^\circ$  produces an almost equally good fit ( $\chi^2$  reduced by only 4%). Such a relatively small, low latitude hot spot would show a large RV modulation ( $10 \text{ km s}^{-1}$  peak to peak) that is  $180^\circ$  out of phase with the photospheric RV measurements, producing an inverse correlation between the photospheric RV measurements and RV measurements for emission lines coming from the hot spot. We looked for this behavior in the NCs of the He I 5876 Å and Ca II 8662 Å lines.

The RV signals of these two emission lines are plotted versus the optical photospheric RV measurements in the top two panels of Figure 11. We performed correlation analyses using both the linear correlation coefficient and the Spearman’s and Kendal’s  $\tau$  rank order correlation coefficients. No correlation was observed. The most significant correlation with the photospheric RVs is for the RV measurements of the He I line, but the false alarm probability is 0.58 for Kendal’s  $\tau$  and higher still for the other statistics. We also performed a periodogram analysis on the emission line RV measurements and the veiling measurements, as well as phase folding these to the 8.9965 and 8.9891 d periods. In all cases, no significant signal was found. As a result, there is no evidence that a hot spot is producing the RV signals seen in the photospheric absorption lines, and long term photometric measurements do not show the signal expected from a long lived coherent hot spot if it were responsible for the observed RV variations in CI Tau. Thus, we suggest that it is unlikely that a hot spot is responsible for the photospheric RV signals seen in this star.

## 4.2. Scattering off an Inner Disk Wall

CI Tau is a CTTS surrounded by a circumstellar accretion disk. The disk mass for CI Tau has been estimated by several authors (Andrews & Williams 2005, 2007; Mohanty et al. 2013; McClure et al. 2013) with values that range from  $18.7 M_{Jup}$  (Mohanty et al. 2013) to  $71.3 M_{Jup}$  (McClure et al. 2013). McClure et al. (2013) estimate that the inner disk of CI Tau is truncated at a radius of 0.12 AU, which is close to the apastron distance (0.10 AU assuming  $e = 0.28$ ) of the suspected planet found in our RV analysis. The inner disk can scatter incident starlight, adding a scattered light spectrum to the directly observed spectrum of the star. Such a scattered light spectrum was detected in the optical for the spectroscopic binary star KH 15D by Herbst et al. (2008). These authors find that the reflected light from the disk is about 3% of the direct spectrum in the optical near 6000 Å, and that the

reflected component can cause measurable effects on optical line profiles at certain phases in the binary orbit. For a single star with an azimuthally symmetric disk, this type of scattering should produce a symmetric reflected light line profile centered on the stellar line, and would not therefore be expected to produce any apparent RV shift. However, the inner walls of circumstellar disks are believed to be warped or otherwise not symmetric in many cases, resulting in detectable photometric variability (e.g. Cody et al. 2014; Stauffer et al. 2014; McGinnis et al. 2015). If there is some coherent structure at or near the inner wall of the accretion disk, it might contribute a scattered light component that is Doppler shifted along our line of sight relative to the star as a result of the orbital motion of the disk. As the structure orbits the star, its velocity shift relative to the star would change, potentially distorting the photospheric absorption lines and creating an apparent velocity signal for the star.

For a structure at the inner wall of the disk to be responsible for the observed RV signatures above, it must be located at a distance where the period is equal to 8.99 days. For the  $0.80 M_{\odot}$  mass of CI Tau, this corresponds to 0.079 AU, well inside the 0.12 AU inner wall of the disk found by McClure et al. (2013). Looking at it another way, the orbital period at 0.12 AU is 17 days, substantially longer than the period of RV variations. In order to produce the observed RV variations, such a disk structure would need to remain stable over the 9 year span of the data collected here. Such stability is unlikely given the short dynamical time of the disk at this radius, unless the disk structure, such as a warp, is excited and maintained by some other object or process. A massive planet inside the disk gap could excite such a disk structure. The interaction of the inner disk wall with the stellar magnetosphere, particularly if the magnetosphere is tilted, could also excite a long term stable disk warp as is believed to be the case for AA Tau for example (Bouvier et al. 2003, 2013). Such a disk warp is tied to the stellar rotation, which our photometric monitoring suggests has a period of  $\sim 7$  days instead of 9 days. Another estimate for the rotation period of CI Tau can be made using its  $v \sin i$ , stellar radius, and inclination. Assuming the inclination of the star is equal to that of the disk, we can use  $i = 55^{\circ}$  and  $R_* = 1.41 R_{\odot}$  (both from McClure et al. 2013). Taking  $v \sin i = 11 \text{ km s}^{-1}$  again from Basri and Batalha (1990), the rotation period is estimated to be 5.3 days. This estimate shrinks somewhat to 4.6 days using the inclination of  $45.7^{\circ}$  degrees from Guilloteau et al. (2014), and  $i = 90$  gives an estimated period of 6.5 days. There are of course uncertainties in the stellar radius and  $v \sin i$ , so these period estimates are themselves uncertain; however, the available measurements point to a rotation period noticeably less than the 8.99 day period of the RV variations.

While the estimates above argue that some sort of structure in the inner disk wall scattering starlight from CI Tau is probably not responsible for the RV variations we measure, we can look to the data for evidence one way or another. The spectral model used to



measure the K band RVs in §3.1 includes a term that measures the strength of the 2.29  $\mu\text{m}$  K band photospheric lines which can vary as the result of veiling, a measure of the continuum emission from the inner disk relative to that from the star (e.g. Folha & Emerson 1999; Johns-Krull & Valenti 2001). If there is a coherent structure in the inner disk responsible for scattering starlight and producing the observed RV variations, we might expect there to be a correlation between the K band veiling and the measured RVs. We convert our measurements into the K band veiling (measured at 2.29  $\mu\text{m}$  as opposed to averaged over the entire band), referenced to the model spectrum used in the fitting process. These K band veilings are reported in Table 1. We phase the K band veilings with respect to the 8.99 day RV period in Figure 12, but we find no apparent pattern with the phase. We also computed the periodogram of the K band veiling measurements, finding no significant peaks near 9 days. In particular, the false alarm probability of the highest peak within  $\pm 5$  days of 8.99 days is 0.81, with the period of the peak being 13.6 days. Thus, our IR observations do not show any relationship between the disk emission and the measured RVs.

We can also estimate the level of scattering that would be needed to produce the observed RV signal. As mentioned above, in order to produce periodicity at  $\sim 9$  days, the scattering surface in the disk would need to be at radius of  $\sim 0.08$  AU where the Keplerian velocity is  $\sim 96$   $\text{km s}^{-1}$ . Using  $i = 45.^\circ 7$ , this surface would vary in RV by  $\pm 68$   $\text{km s}^{-1}$  relative to the star. As the lines in the scattered light spectrum move through the stellar spectrum, they can distort the photospheric line profile and appear to produce a velocity shift. We estimate the strength of the required scattered light spectrum by asking how strong the scattered light line profile would need to be relative to the stellar lines in order to produce the  $\pm 1$   $\text{km s}^{-1}$  shift that is observed in the RV signal (Figure 4). We first assumed the scattered light spectral lines are identical to those in the star. This assumes the scattering source is essentially a point in the disk so that the reflected stellar spectrum is not smeared in velocity space because of formation around a range in azimuth in the disk. We used the the LSD Stokes I photospheric profiles calculated for the optical spectra in §3.2 and added a scaled version of the same spectrum to the original profile shifted by a specified RV value. We stepped through shifts of  $\pm 68$   $\text{km s}^{-1}$  in  $0.1$   $\text{km s}^{-1}$  steps and used the same cross correlation technique as in §3.2 to measure the resulting RV shift. We find that in order to produce a maximum line distortion of  $\pm 1$   $\text{km s}^{-1}$ , the scattered light spectrum needs to be  $\sim 17\%$  the strength of the directly observed stellar spectrum (Figure 13). If this were indeed occurring, a feature 17% as deep as the observed profiles would be present in the spectra of CI Tau and would move periodically back and forth relative to the main lines by  $\pm 68$   $\text{km s}^{-1}$ . Such a feature would be obvious in the LSD optical profiles (Figure 13) and is not seen. If we instead represent the scattered light spectrum as the stellar spectrum convolved with a Gaussian of  $\text{FWHM} = 40$   $\text{km s}^{-1}$  to mimic scattering from a range of

disk azimuth, we find that the scattered light component must be  $\sim 57\%$  as strong as the stellar spectrum in order to produce the measured RV variations. Such a strong component is not seen in the observed spectra, and this high level of scattering is also unphysical (e.g. Whitney & Hartmann 1992). We conclude it is highly unlikely that scattering off the inner disk is producing the RV variations we observe.

### 4.3. The Challenge and Necessity of Finding Planets Around CTTSs

We conclude that the best interpretation of the data presented in this paper is that there is an  $\sim 11 - 12 M_{JUP}$  mass planet on a somewhat eccentric  $\sim 9$  d orbit around the CTTS CI Tau. We have illustrated some of the unique difficulties in searching for planets around actively accreting, young stars. However, in order to understand planet formation, it will be necessary to look for planets in just such systems. All indications of the thousands of planets identified by the *Kepler* mission, as well as the structure and likely dynamic history of our own solar system, point to significant evolution and migration of planets, including the gas giants (e.g., Levison et al. 2007). In order to begin to document and characterize the extent of these processes, and to determine the nature of planet formation itself, we are compelled to search for the first generation of planets around host stars with extreme and variable properties.

Classical T Tauri stars undergoing active accretion present complex challenges for the identification of even giant planets on short period orbits. Some of these have been described above. Potential sources of variable photometry include changes in geometry and extinction resulting from modifications in the line of sight across or through the circumstellar disk as it rotates. Furthermore, bright accretion footprints and episodic accretion events, cool stellar spots, stellar flares, massive coronal mass ejections, stellar jet outbursts, among other phenomena, may all contribute to a particularly high level of activity and thus variability. Spectral absorption line profile variability may result from the shift in an absorption line center as a large dark spot (or spots) is carried across the observed stellar hemisphere by the star’s own rotation. Hot spots from accretion or flares on the stellar surface may produce an analogous result. Accreting hot gas, and warm dust grains in the inner disk, may give rise to a continuum excess which veils absorption lines and can, in extreme cases, effectively obliterate them. Strong variability in emission line fluxes and line profiles result from excitation arising in clumpy accretion flows, stellar winds, and jets (e.g., Alencar et al. 2005). Yet it is at this tumultuous phase in a star’s lifetime during which planets must have already formed or be in the formation process, given the relatively short window of availability of the reservoir of raw material in the primordial disk.

The evidence we present for a giant planet in the CI Tau system is demonstrated on the basis of diverse data sets collected over 10 years at 5 different facilities. Over this multi-year time scale we find consistent variability in the IR RVs, as well as evidence in the optical RV variations, for this same periodic signal, supporting our planetary companion interpretation. Some significant scatter is obvious in the IR RVs plotted in Figures 2 and 4; we interpret this as likely the result of astrophysical processes, such as those described above. Although working in the IR diminishes the impact of cool star spots and stellar activity, it does not guarantee immunity from these phenomena, particularly in a classical T Tauri system. Some processes, such as emission from warm grains in an inner circumstellar disk, may wield a greater impact in the IR. However, although this work is outside the scope of this current paper, we are hopeful that it will be possible to minimize these sources of interference in our RV measurements. For example, for stars with known rotation periods, specific observing allocations in the future can be used to tailor the IR spectroscopic observations to take place repeatedly at the same rotational phase of the star (e.g., Robertson et al. 2015), thus nulling any spot signal. We can also experiment with spot modeling in order to determine the degree of interference anticipated in our IR RV measurements, and with extracting contaminating spot signals from our spectra directly (e.g., Moulds et al. 2012; Llama et al. 2012; Bradshaw & Hartigan 2014; Aigrain et al. 2015).

The behavior of activity on young stars is not well understood. Astronomers know that extreme cases are possible, for example unusually long lived spots which appear to phase coherently over many years (Stelzer et al. 2003; Mahmud et al. 2011; Bradshaw & Hartigan 2014), or spots with filling factors that cover most of the stellar surface (Hatzes 1995). Although T Tauri stars are all presumed to have strong magnetic fields and corresponding activity (Johns–Krull 2007), it is not uncommon to find systems which defy characterization of their rotation periods on the basis of spots (e.g., Xiao et al. 2012). Classical T Tauri stars, with their many types of potential activity, are among the most difficult for the measurement of rotation, although many show variable behavior which at times reveals periodic light curve behavior (Herbst et al. 2002). CI Tau appears to fit into this category. The peculiar activity that distinguishes CTTSs is embodied by the  $H\alpha$  line and its variations. This line is a strong accretion diagnostic, and the  $H\alpha$  variability of CI Tau is intriguing. The red side of the profile shows potentially periodic variability that phases well with the orbital period of the likely planetary companion (Figure 8). The exact cause of this variability is not clear however. The  $H\alpha$  luminosity of accreting roughly planetary mass objects may be as high as 10% that of the central star (e.g., Zhou et al. 2014), so it is possible this variability results from the RV motion of  $H\alpha$  emission associated with the planet itself. In that case, one would expect similar periodicity at all velocities sampled by the planetary orbit, as long as they are strong enough relative to the line profile variations from the star itself. It is also

possible that this apparent periodicity in the H $\alpha$  line is caused by the planet modulating the accretion of disk material onto the star, similar to that seen in close, eccentric binary CTTSs like DQ Tau (e.g., Basri et al. 1997). In either case, the H $\alpha$  variability of CI Tau deserves further investigation.

The definitive characterization of a massive planet in the CI Tau system will require continued monitoring for an RV signal in the IR consistent with the orbital parameters identified to date and corroborating results from optical RV observations, modulo potentially variable cool spot noise. A firm detection of the photometric rotation period with a period different from the RV period would also help substantiate the existence of a planet orbiting CI Tau. Verification of our result must necessarily rely for now on these ground-based techniques as the candidate CI Tau planet will not be astrometrically detectable by the GAIA mission, for example (Sozzetti et al. 2014).

## 5. Summary

We have identified a  $\sim 9$  day period in the K band RV variations of the classical T Tauri star CI Tau. The best interpretation of these data is that a massive planet is in orbit around this young star located in the Taurus star forming region. This identification is based on high-resolution IR spectroscopy supported by high-resolution optical spectroscopy and optical photometry, all collected over a 10 year total time span. For the  $\sim 5$  years of our IR observations of CI Tau, from 2009 to 2014, the RVs extracted from the spectroscopy phase to a period of  $\sim 9$  days. While not sufficient to independently confirm the  $\sim 9$  day period, the full set of optical RVs also phase reasonably well to the  $\sim 9$  day RV period observed in the IR spectroscopy. While it is expected that the optical RV measurements experience a greater impact from cool starspots than the IR RVs, the amplitude of the optical RV variations is very similar to those observed in the IR, indicating that noise from cool spots does not obliterate the planetary signal. We also investigate the possibility that the observed photospheric RV variations on this CTTS result from an accretion hot spot or from scattering off the inner wall of the accretion disk. These scenarios gives rise to a few potentially testable predictions which are not supported by the data collected here or by other investigators. Therefore, we find that the best interpretation of the observations presented here is that the RV variability of CI Tau results from reflex motion induced by a  $\sim 11\text{--}12 M_{Jup}$  planet. Furthermore, we find that the flux in the  $+200 \text{ km s}^{-1}$  region of CI Tau’s H $\alpha$  emission line varies with an apparent periodicity of  $\sim 9$  days, suggestive of detection of accretion onto the planet at a particular orbital phase. While the period of  $\sim 9$  days is strongly detected in our data, the large level of astrophysical noise means that some

of the orbital parameters (e.g., the eccentricity) are not well determined. A firmer detection of the rotation period of the star is also needed. As a result, more observations of CI Tau are critical to confirm this important result, as well as additional observations to detect giant planets around other young stars. An excess in the *young* hot Jupiter population may indicate the prevalence of destructive mechanisms which result in the relative paucity of massive, short-period planets around main-sequence stars,  $\sim 1\%$  (e.g., Wright et al. 2012). A massive planet in a  $\sim 9$  period day orbit around a 2 Myr old star places strong constraints on planet formation and migration time scales. It is key to our understanding of exoplanet evolution to determine how common such systems are.

We thank the IRTF TOs Dave Griep, Bill Golisch, and Eric Volquardsen and SAs John Rayner, Mike Connelly, and Bobby Bus, the Keck Observatory OAs Cynthia Wilburn and Heather Hershley and SAs Scott Dahm and Greg Wirth, KPNO staff Dave Summers, Di Harmer, and Dick Joyce, and Dave Doss of McDonald Observatory for their exceptional observing support over the many years of this program. LP is grateful to Peter Bodenheimer, Joe Llama, Evgenya Shkolnik, and Ben Zuckerman for insightful discussions. Partial support for this research was provided by the SIM Young Planets Key Project and by NASA Origins grants 05-SSO05-86 and 07-SSO07-86 to LP. Additional support for this work was provided by the NSF through grant AST-1212122 made to Rice University. We are grateful to the Arizona Space Grant consortium for support of JNM’s participation in this work. We wish to thank an anonymous referee for many helpful comments that improved the manuscript. This work made use of the SIMBAD reference database, the NASA Astrophysics Data System, and the data products from the Two Micron All Sky Survey, which is a joint project of the University of Massachusetts and the Infrared Processing and Analysis Center/California Institute of Technology, funded by the National Aeronautics and Space Administration and the National Science Foundation. This work made use of the Immersion Grating Infrared Spectrograph (IGRINS) that was developed under a collaboration between the University of Texas at Austin and the Korea Astronomy and Space Science Institute (KASI) with the financial support of the US National Science Foundation under grant AST-1229522, of the University of Texas at Austin, and of the Korean GMT Project of KASI. Some data presented herein were obtained at the W. M. Keck Observatory, which is operated as a scientific partnership among the California Institute of Technology, the University of California, and the National Aeronautics and Space Administration. The Observatory was made possible by the generous financial support of the W. M. Keck Foundation. The authors recognize and acknowledge the significant cultural role that the summit of Mauna Kea plays within the indigenous Hawaiian community. We are grateful for the opportunity to conduct observations from this special mountain.

## REFERENCES

- Alencar, S. H. P., & Basri, G. 2000, *AJ*, 119, 1881
- Alencar, S. H. P., Basri, G., Hartmann, L., & Calvet, N. 2005, *A&A*, 440, 595
- Aigrain, S., Llama, J., Ceillier, T., et al. 2015, *MNRAS*, 450, 3211
- Andrews, S. M., & Williams, J. P. 2005, *ApJ*, 631, 1134
- Andrews, S. M., & Williams, J. P. 2007, *ApJ*, 659, 705
- Apai, D., Schneider, G., Grady, C. A., et al. 2015, *ApJ*, 800, 136
- Armitage, P.J. & Bonnell, I.A. 2002, *MNRAS*, 330, L11
- Artemenko, S. A., Grankin, K. N., & Petrov, P. P. 2012, *Astronomy Letters*, 38, 783
- Bailey, J. I., III, White, R. J., Blake, C. H., et al. 2012, *ApJ*, 749, 16
- Basri, G., & Batalha, C. 1990, *ApJ*, 363, 654
- Basri, G., Johns-Krull, C. M., & Mathieu, R. D. 1997, *AJ*, 114, 781
- Batalha, C. C., Stout-Batalha, N. M., Basri, G., & Terra, M. A. O. 1996, *ApJS*, 103, 211
- Batalha, C., Batalha, N. M., Alencar, S. H. P., Lopes, D. F., & Duarte, E. S. 2002, *ApJ*, 580, 343
- Bean, J. L., Seifahrt, A., Hartman, H., et al. 2010, *ApJ*, 713, 410
- Blake, C. H., Charbonneau, D., & White, R. J. 2010, *ApJ*, 723, 684
- Bergin, E. A., Cleeves, L. I., Gorti, U., et al. 2013, *Nature*, 493, 644
- Beristain, G., Edwards, S., & Kwan, J. 2001, *ApJ*, 551, 1037
- Bevington, P. R., & Robinson, D. K. 1992, New York: McGraw-Hill, —c1992, 2nd ed.
- Bouvier, J., Grankin, K. N., Alencar, S. H. P., et al. 2003, *A&A*, 409, 169
- Bouvier, J., Grankin, K., Ellerbroek, L. E., Bouy, H., & Barrado, D. 2013, *A&A*, 557, A77
- Bowler, B. P., Liu, M. C., Shkolnik, E. L., & Dupuy, T. J. 2013, *ApJ*, 774, 55
- Bradshaw, S. J., & Hartigan, P. 2014, *ApJ*, 795, 79

- Butler, R. P., Marcy, G. W., Williams, E., et al. 1996, *PASP*, 108, 500
- Calvet, N., & Gullbring, E. 1998, *ApJ*, 509, 802
- Cauley, P. W., Johns-Krull, C. M., Hamilton, C. M., & Lockhart, K. 2012, *ApJ*, 756, 68
- Chauvin, G., Lagrange, A.-M., Dumas, C., et al. 2004, *A&A*, 425, L29
- Chauvin, G., Lagrange, A.-M., Dumas, C., et al. 2005, *A&A*, 438, L25
- Chen, W., & Johns-Krull, C. M. 2013, *ApJ*, 776, 113
- Ciardi, D. R., van Eyken, J. C., Barnes, J. W., et al. 2015, *ApJ*, 809, 42
- Cody, A. M., Stauffer, J., Baglin, A., et al. 2014, *AJ*, 147, 82
- Crockett, C. J., Mahmud, N. I., Prato, L., et al. 2011, *ApJ*, 735, 78
- Crockett, C. J., Mahmud, N. I., Prato, L., et al. 2012, *ApJ*, 761, 164
- Davison, C. L., White, R. J., Henry, T. J., et al. 2015, *AJ*, 149, 106
- Delorme, P., Gagné, J., Girard, J. H., et al. 2013, *A&A*, 553, L5
- Desort, M., Lagrange, A.-M., Galland, F., Udry, S., & Mayor, M. 2007, *A&A*, 473, 983
- Donati, J.-F., Semel, M., Carter, B. D., Rees, D. E., & Collier Cameron, A. 1997, *MNRAS*, 291, 658
- Donati, J.-F., Jardine, M. M., Gregory, S. G., et al. 2008, *MNRAS*, 386, 1234
- Donati, J.-F., Skelly, M. B., Bouvier, J., et al. 2010, *MNRAS*, 409, 1347
- Droege, T. F., Richmond, M. W., Sallman, M. P., & Creager, R. P. 2006, *PASP*, 118, 1666
- Fabrycky, D., & Tremaine, S. 2007, *ApJ*, 669, 1298
- Figueira, P., Pepe, F., Lovis, C., & Mayor, M. 2010, *A&A*, 515, A106
- Fischer, W. J., Megeath, S. T., Tobin, J. J., et al. 2012, *ApJ*, 756, 99
- Folha, D. F. M., & Emerson, J. P. 1999, *A&A*, 352, 517
- Goorvitch, D. 1994, *ApJS*, 95, 535
- Graham, J. A. 1992, *PASP*, 104, 479

- Grankin, K. N., Melnikov, S. Y., Bouvier, J., Herbst, W., & Shevchenko, V. S. 2007, *A&A*, 461, 183
- Greene, T. P., Tokunaga, A. T., Toomey, D. W., & Carr, J. B. 1993, *Proc. SPIE*, 1946, 313
- Gullbring, E., Hartmann, L., Briceño, C., & Calvet, N. 1998, *ApJ*, 492, 323
- Guilloteau, S., Simon, M., Piétu, V., et al. 2014, *A&A*, 567, A117
- Hartigan, P., Hartmann, L., Kenyon, S., Hewett, R., & Stauffer, J. 1989, *ApJS*, 70, 899
- Hartigan, P., Kenyon, S. J., Hartmann, L., et al. 1991, *ApJ*, 382, 617
- Harris, A. W., Young, J. W., Bowell, E., et al. 1989, *Icarus*, 77, 171
- Hatzes, A. P. 1995, *ApJ*, 451, 784
- Hauschildt, P. H., Allard, F., & Baron, E. 1999, *ApJ*, 512, 377
- Henden, A., & Munari, U. 2014, *Contributions of the Astronomical Observatory Skalnaté Pleso*, 43, 518
- Herbst, W., Bailer-Jones, C. A. L., Mundt, R., Meisenheimer, K., & Wackermann, R. 2002, *A&A*, 396, 513
- Herbst, W., Hamilton, C. M., Leduc, K., et al. 2008, *Nature*, 452, 194
- Hillenbrand, L. A., Miller, A. A., Covey, K. R., et al. 2013, *AJ*, 145, 59
- Hinkle, K. H., Cuberly, R. W., Gaughan, N. A., et al. 1998, *Proc. SPIE*, 3354, 810
- Hinkle, K., Wallace, L., Valenti, J., & Harmer, D. 2000, *Visible and Near Infrared Atlas of the Arcturus Spectrum 3727-9300 Å* ed. Kenneth Hinkle, Lloyd Wallace, Jeff Valenti, and Dianne Harmer. (San Francisco: ASP) ISBN: 1-58381-037-4, 2000.
- Horne, K. 1986, *PASP*, 98, 609
- Horne, J. H., & Baliunas, S. L. 1986, *ApJ*, 302, 757
- Howarth, I. D. 2016, *MNRAS*, 457, 3769
- Huélamo, N., Figueira, P., Bonfils, X., et al. 2008, *A&A*, 489, L9
- Huerta, M., Johns-Krull, C. M., Prato, L., Hartigan, P., & Jaffe, D. T. 2008, *ApJ*, 678, 472



- Ireland, M. J., Kraus, A., Martinache, F., Law, N., & Hillenbrand, L. A. 2011, *ApJ*, 726, 113
- Ireland, M. J., & Kraus, A. L. 2014, *IAU Symposium*, 299, 199
- Johns, C. M., & Basri, G. 1995, *ApJ*, 449, 341
- Johns-Krull, C. M. 2007, *ApJ*, 664, 975
- Johns-Krull, C. M., & Valenti, J. A. 2001, *ApJ*, 561, 1060
- Johns-Krull, C. M., Valenti, J. A., Hatzes, A. P., & Kanaan, A. 1999, *ApJ*, 510, L41
- Klinglesmith, D. A., III 2012, *Minor Planet Bulletin*, 39, 109
- Kóspál, Á., Mohler-Fischer, M., Sicilia-Aguilar, A., et al. 2014, *A&A*, 561, A61
- Kraus, A. L., & Ireland, M. J. 2012, *ApJ*, 745, 5
- Kraus, A. L., Ireland, M. J., Cieza, L. A., et al. 2014, *ApJ*, 781, 20
- Kulkarni, A. K., & Romanova, M. M. 2008, *MNRAS*, 386, 673
- Kupka, F. G., Ryabchikova, T. A., Piskunov, N. E., Stempels, H. C., & Weiss, W. W. 2000, *Baltic Astronomy*, 9, 590
- Kurosawa, R., & Romanova, M. M. 2013, *MNRAS*, 431, 2673
- Lafrenière, D., Jayawardhana, R., & van Kerkwijk, M. H. 2008, *ApJ*, 689, L153
- Levison, H. F., Morbidelli, A., Gomes, R., & Backman, D. 2007, *Protostars and Planets V*, 669
- Livingston, W., & Wallace, L. 1991, *NSO Technical Report*, Tucson: National Solar Observatory, National Optical Astronomy Observatory, 1991
- Llama, J., Jardine, M., Mackay, D. H., & Fares, R. 2012, *MNRAS*, 422, L72
- Luhman, K. L., Wilson, J. C., Brandner, W., et al. 2006, *ApJ*, 649, 894
- Mahmud, N. I., Crockett, C. J., Johns-Krull, C. M., et al. 2011, *ApJ*, 736, 123
- Marcy, G.W. & Butler, R.P. 2000, *PASP*, 112, 137
- Marois, C., Zuckerman, B., Konopacky, Q. M., Macintosh, B., & Barman, T. 2010, *Nature*, 468, 1080

- Martín, E. L., Guenther, E., Zapatero Osorio, M. R., Bouy, H., & Wainscoat, R. 2006, *ApJ*, 644, L75
- McClure, M. K., D’Alessio, P., Calvet, N., et al. 2013, *ApJ*, 775, 114
- McGinnis, P. T., Alencar, S. H. P., Guimarães, M. M., et al. 2015, *A&A*, 577, A11
- Mohanty, S., Greaves, J., Mortlock, D., et al. 2013, *ApJ*, 773, 168
- Moulds, V., & Watson, C. 2010, *IAC Talks, Astronomy and Astrophysics Seminars from the Instituto de Astrofísica de Canarias*, 225
- Nelder, J. & Mead, R. 1965, *Comput. J.*, 7, 308
- Neuhäuser, R., Guenther, E. W., Wuchterl, G., et al. 2005, *A&A*, 435, L13
- Neuhäuser, R., Mugrauer, M., Seifahrt, A., et al. 2008, *A&A*, 484, 281
- Park, C., Jaffe, D. T., Yuk, I.-S., et al. 2014, *Proc. SPIE*, 9147, 91471D
- Partnership, A., Brogan, C. L., Perez, L. M., et al. 2015, *arXiv:1503.02649*
- Percy, J. R., Grynko, S., Seneviratne, R., & Herbst, W. 2010, *PASP*, 122, 753
- Piskunov, N. 1999, *Polarization*, 243, 515
- Piskunov, N. E., & Valenti, J. A. 2002, *A&A*, 385, 1095
- Pojmanski, G. 1997, *Acta Astron.*, 47, 467
- Prato, L., Huerta, M., Johns-Krull, C. M., et al. 2008, *ApJ*, 687, L103
- Quinn, S. N., White, R. J., Latham, D. W., et al. 2014, *ApJ*, 787, 27
- Ragozzine, D., & Kepler Team 2012, *AAS/Division for Planetary Sciences Meeting Abstracts*, 44, #200.04
- Reiners, A., Bean, J. L., Huber, K. F., et al. 2010, *ApJ*, 710, 432
- Robertson, P., Roy, A., & Mahadevan, S. 2015, *ApJ*, 805, L22
- Romanova, M. M., Kulkarni, A. K., & Lovelace, R. V. E. 2008, *ApJ*, 673, L171
- Saar, S. H., & Donahue, R. A. 1997, *ApJ*, 485, 319
- Sallum, S., Follette, K. B., Eisner, J. A., et al. 2015, *Nature*, 527, 342

- Schmidt, T. O. B., Neuhäuser, R., Seifahrt, A., et al. 2008, *A&A*, 491, 311
- Schneider, A., Melis, C., & Song, I. 2012, *ApJ*, 754, 39
- Setiawan, J., Henning, T., Launhardt, R., et al. 2008, *Nature*, 451, 38
- Sicilia-Aguilar, A., Fang, M., Roccatagliata, V., et al. 2015, arXiv:1505.08011
- Simon, M., Schlieder, J. E., Constantin, A.-M., & Silverstein, M. 2012, *ApJ*, 751, 114
- Sozzetti, A., Giacobbe, P., Lattanzi, M. G., et al. 2014, *MNRAS*, 437, 497
- Stauffer, J., Cody, A. M., Baglin, A., et al. 2014, *AJ*, 147, 83
- Stelzer, B., Fernández, M., Costa, V. M., et al. 2003, *A&A*, 411, 517
- Su, K. Y. L., Rieke, G. H., Stapelfeldt, K. R., et al. 2009, *ApJ*, 705, 314
- Tokunaga, A. T., Toomey, D. W., Carr, J., Hall, D. N. B., & Epps, H. W. 1990, *Proc. SPIE*, 1235, 131
- Tull, R. G., MacQueen, P. J., Sneden, C., & Lambert, D. L. 1995, *PASP*, 107, 251
- Valenti, J. A. 1994, Ph.D. Thesis, University of California, Berkeley
- Valenti, J. A., Basri, G., & Johns, C. M. 1993, *AJ*, 106, 2024
- van Eyken, J. C., Ciardi, D. R., von Braun, K., et al. 2012, *ApJ*, 755, 42
- Whitney, B. A., & Hartmann, L. 1992, *ApJ*, 395, 529
- Wolszczan, A., & Frail, D. A. 1992, *Nature*, 355, 145
- Wright, J. T., Marcy, G. W., Howard, A. W., et al. 2012, *ApJ*, 753, 160
- Xiao, H. Y., Covey, K. R., Rebull, L., et al. 2012, *ApJS*, 202, 7
- Yu, L., Winn, J. N., Gillon, M., et al. 2015, *ApJ*, 812, 48
- Zhou, Y., Herczeg, G. J., Kraus, A. L., Metchev, S., & Cruz, K. L. 2014, *ApJ*, 783, L17

Table 1. CI Tau Infrared Spectroscopy

Julian Date	RV (km s <sup>-1</sup> )	$\sigma_{RV}$ (km s <sup>-1</sup> )	$r_K$	$\sigma_{r_K}$
CSHELL				
2455156.098	-0.02	0.21	2.33	0.17
2455158.116	-0.33	0.20	1.84	0.12
2455160.107	-0.62	0.14	2.46	0.11
2455235.900	-0.49	0.24	1.94	0.16
2455236.851	-0.07	0.16	2.37	0.12
2455237.879	0.40	0.14	1.90	0.08
2455238.884	1.06	0.14	1.64	0.07
2455239.892	1.26	0.12	1.57	0.05
2455240.889	0.27	0.23	1.49	0.11
2455241.866	0.70	0.14	1.46	0.06
2455242.863	0.52	0.13	1.56	0.05
2456258.027	0.45	0.16	1.55	0.07
2456258.945	-1.02	0.18	1.62	0.09
2456259.117	-1.40	0.22	2.30	0.17
2456259.840	-0.48	0.11	1.38	0.04
2456260.879	-0.76	0.14	1.49	0.06
2456263.769	0.28	0.13	1.19	0.04
2456622.774	-0.61	0.08	0.00	0.01
2456623.785	0.14	0.10	0.13	0.01
2456624.859	1.01	0.11	0.77	0.03
2456625.881	0.88	0.19	1.11	0.02
2456626.911	0.16	0.40	0.97	0.10
2456690.895	-0.29	0.31	0.35	0.02
2456693.750	-0.45	0.63	1.51	0.40
2456696.769	0.74	0.15	0.95	0.08
2456697.773	0.20	0.17	0.94	0.05
2456698.747	0.13	0.46	0.90	0.14
2456699.748	0.08	0.14	0.93	0.05
2456701.745	-0.52	0.40	1.05	0.06

Table 1—Continued

Julian Date	RV (km s <sup>-1</sup> )	$\sigma_{RV}$ (km s <sup>-1</sup> )	$r_K$	$\sigma_{r_K}$
2456714.739	0.67	0.10	0.94	0.01
2456715.737	1.98	0.22	0.98	0.03
2456716.743	-0.03	0.23	0.98	0.07
2456717.741	1.22	0.34	0.86	0.06
2456723.740	0.75	0.33	0.51	0.01
NIRSPEC				
2455251.727	-0.14	0.07	1.49	0.03
2455255.730	-0.86	0.05	1.64	0.03
2455522.880	-0.26	0.05	1.73	0.03
Phoenix				
2456350.633 <sup>a</sup>	-1.24	0.06	0.34	0.01
2456351.614 <sup>a</sup>	-1.29	0.07	0.41	0.01
2456352.610 <sup>a</sup>	-0.42	0.06	0.40	0.01
2456353.607 <sup>a</sup>	0.27	0.07	0.45	0.01
2456354.668 <sup>a</sup>	0.27	0.07	0.22	0.01
2456605.732	-0.56	0.06	0.13	0.01
2456606.810	0.48	0.06	0.33	0.01
2456607.778	1.40	0.07	0.29	0.01
2456608.761	0.88	0.07	0.26	0.01
2456610.769	-1.41	0.06	0.26	0.01
2456643.930	1.32	0.07	0.00	0.01
2456644.875	-1.18	0.13	0.08	0.01
2456645.771	0.31	0.08	0.41	0.01
2456661.857	2.60	0.16	0.53	0.01
2456662.840	-2.01	0.13	0.48	0.01
2456663.817	-0.73	0.08	0.29	0.01
2456664.723	-1.01	0.07	0.48	0.01
2456666.708	-0.79	0.07	0.41	0.01

Table 1—Continued

Julian Date	RV (km s <sup>-1</sup> )	$\sigma_{RV}$ (km s <sup>-1</sup> )	$r_K$	$\sigma_{r_K}$
2456667.791	-0.49	0.07	0.24	0.01
IGRINS				
2456925.895	-0.89	0.32	1.45	0.01
2456940.827	2.14	0.32	1.18	0.04
2456984.776	0.90	0.34	1.29	0.07
2456985.924	-0.04	0.15	0.88	0.03
2456986.908	0.95	0.20	0.87	0.04
2456987.851	-1.03	0.31	1.08	0.05
2456988.855	0.36	0.13	1.33	0.03
2456989.788	-1.07	0.13	1.56	0.01
2456990.813	-1.19	0.27	1.45	0.07
2456991.704	-1.42	0.23	1.39	0.07
2456992.686	0.87	0.24	1.19	0.04
2456993.745	0.20	0.35	1.38	0.05
2456996.826	0.43	0.21	1.22	0.06
2456997.686	-0.39	0.28	1.70	0.10
2457029.577	-0.77	0.54	1.03	0.07

<sup>a</sup>For these nights, Phoenix was mounted on the KPNO 4-meter; all other Phoenix data were taken with the KPNO 2.1-meter.

Table 2. CI Tau Optical Spectroscopy

Julian Date	RV (km s <sup>-1</sup> )	$\sigma_{RV}$ (km s <sup>-1</sup> )	Ca II RV (km s <sup>-1</sup> )	$\sigma_{CaII}$ (km s <sup>-1</sup> )	He I RV (km s <sup>-1</sup> )	$\sigma_{HeI}$ (km s <sup>-1</sup> )	$r$	$\sigma_r$
2453367.805	-0.46	0.22	19.21	0.46	22.79	0.93	0.09	0.01
2453696.899	-0.03	0.26	17.66	0.24	21.82	0.60	0.12	0.01
2453770.777	1.05	0.25	18.43	0.40	25.19	0.94	0.66	0.02
2454141.782	...	...	16.72	0.40	25.38	0.70	...	...
2454424.950	0.12	0.23	17.49	0.37	15.85	1.22	0.54	0.01
2455159.848	-0.71	0.21	17.89	0.60	19.47	1.51	0.31	0.02
2455160.819	0.59	0.14	17.53	0.53	19.67	0.61	0.79	0.02
2455161.787	0.96	0.20	15.44 <sup>a</sup>	0.31	20.26	0.64	0.94	0.02
2455162.834	-0.72	0.22	17.74	0.41	21.06	1.10	1.02	0.03
2455163.908	-1.32	0.28	18.84	0.35	22.10	1.00	0.75	0.02
2455164.998	-1.75	0.26	15.43 <sup>b</sup>	0.55	23.43	3.05	0.57	0.03
2456251.697	-0.44	0.28	18.44	0.34	21.42	0.72	0.53	0.02
2456252.678	-1.24	0.38	16.00	0.48	22.24	1.01	0.33	0.02
2456253.844	-0.68	0.24	17.23	0.51	19.79	1.08	0.27	0.01
2456254.680	-0.10	0.17	17.90	0.20	21.14	0.81	0.07	0.01
2456255.703	-0.06	0.18	17.65	0.39	22.85	0.80	0.10	0.01
2456256.669	-0.40	0.18	17.61	0.38	26.37	0.99	0.51	0.01
2456257.669	...	...	18.57	0.23	25.68	2.17	...	...
2456257.905	...	...	19.88	0.55	18.70	1.62	...	...
2456605.692	0.22	0.35	18.35	0.26	20.12	0.66	0.03	0.01
2456605.906	-0.06	0.35	19.48	0.29	21.90	0.63	0.00 <sup>c</sup>	0.00
2456606.680	0.76	0.40	17.00	0.33	20.45	0.57	0.17	0.01
2456606.927	0.45	0.34	18.54	0.31	21.73	0.47	0.18	0.01
2456607.678	1.86	0.50	16.88	0.25	21.81	0.52	0.59	0.02
2456607.871	1.04	0.55	18.43	0.33	22.54	0.48	0.37	0.01
2456608.694	1.15	0.66	15.46	0.98	18.41	1.99	0.69	0.04
2456608.743	0.63	0.52	17.92	0.30	22.22	0.64	0.68	0.02
2456608.949	0.61	0.53	17.46 <sup>b</sup>	0.32	21.88	0.66	0.60	0.02
2456611.659	-1.54	0.56	16.86	0.32	20.09	1.04	0.19	0.01

<sup>a</sup>Strong inverse P-Cygni absorption affecting Ca II profile. The Ca II RV likely biased to a lower value.

<sup>b</sup>Weaker inverse P-Cygni absorption affecting Ca II profile. The Ca II RV is possibly biased to a lower value.

<sup>c</sup>Spectrum used as reference for relative veiling measurements. Veiling is 0.0 by definition.



Table 3. CI Tau Photometry

Heliocentric Julian Date	V (mag)	$\sigma_V$ (mag)
2456238.73400	12.883	0.004
2456238.73618	12.886	0.004
2456238.73836	12.885	0.004
2456238.87180	12.919	0.004
2456238.87398	12.921	0.004
2456239.01481	12.919	0.004
2456239.01699	12.917	0.004
2456239.01917	12.919	0.004
2456239.02135	12.917	0.004
2456239.02353	12.918	0.004
2456239.02571	12.907	0.004
2456239.71033	12.971	0.004
2456239.71251	12.977	0.004
2456239.71468	12.975	0.004
2456239.84985	12.984	0.004
2456239.85203	12.978	0.004
2456239.85421	12.983	0.004
2456240.02371	12.978	0.005
2456240.02588	12.969	0.005
2456240.02807	12.961	0.005
2456240.04286	12.979	0.007
2456240.04504	12.976	0.008
2456240.04722	12.975	0.009
2456251.63990	12.863	0.005
2456251.64208	12.865	0.005
2456251.72535	12.824	0.004
2456251.72754	12.822	0.004
2456251.81324	12.938	0.004
2456251.81541	12.943	0.004
2456251.90858	12.964	0.004

Table 3—Continued

Heliocentric Julian Date	V (mag)	$\sigma_V$ (mag)
2456251.91076	12.966	0.004
2456251.97975	12.969	0.004
2456251.98193	12.973	0.004
2456252.01878	12.966	0.004
2456252.02095	12.967	0.004
2456252.04931	12.965	0.007
2456252.05150	12.978	0.008
2456252.63705	12.992	0.005
2456252.63924	12.999	0.005
2456252.72251	12.903	0.004
2456252.72468	12.894	0.004
2456252.81035	12.841	0.004
2456252.81253	12.850	0.004
2456252.90557	12.934	0.004
2456252.90774	12.943	0.004
2456252.97758	12.934	0.004
2456252.97975	12.935	0.004
2456253.01663	12.941	0.004
2456253.01881	12.957	0.004
2456253.04729	12.945	0.005
2456253.04947	12.940	0.006
2456253.64016	12.908	0.006
2456253.64234	12.889	0.006
2456253.72515	12.939	0.005
2456253.72734	12.941	0.005
2456253.81376	12.963	0.004
2456253.81594	12.962	0.004
2456253.90444	13.031	0.004
2456253.90662	13.031	0.004
2456253.97342	13.056	0.006

Table 3—Continued

Heliocentric Julian Date	V (mag)	$\sigma_V$ (mag)
2456254.01777	13.064	0.004
2456254.01995	13.060	0.004
2456254.04838	13.081	0.006
2456254.05056	13.068	0.007
2456254.63743	13.172	0.006
2456254.63961	13.172	0.006
2456254.72235	13.201	0.005
2456254.72453	13.205	0.005
2456254.81096	13.219	0.005
2456254.81314	13.217	0.005
2456254.90172	13.235	0.004
2456254.90390	13.240	0.004
2456254.96857	13.243	0.004
2456254.97074	13.243	0.004
2456255.01516	13.253	0.004
2456255.01734	13.256	0.004
2456255.04579	13.237	0.005
2456255.04796	13.225	0.006
2456255.62647	13.244	0.007
2456255.62865	13.250	0.006
2456255.71147	13.260	0.005
2456255.71365	13.266	0.005
2456255.79863	13.254	0.005
2456255.80081	13.258	0.005
2456255.90262	13.279	0.005
2456255.90481	13.280	0.005
2456255.96618	13.279	0.004
2456255.96836	13.281	0.004
2456256.00508	13.291	0.004
2456256.00725	13.286	0.004

Table 3—Continued

Heliocentric Julian Date	V (mag)	$\sigma_V$ (mag)
2456256.04240	13.284	0.005
2456256.04458	13.287	0.005
2456256.64926	13.070	0.008
2456256.65144	13.062	0.008
2456256.75939	13.077	0.006
2456256.76157	13.074	0.006
2456256.87745	13.011	0.006
2456256.87963	13.008	0.006
2456256.96075	13.031	0.006
2456256.96293	13.030	0.006
2456257.03305	13.028	0.005
2456257.03523	13.041	0.005
2456267.62628	12.954	0.007
2456267.62846	12.970	0.007
2456267.69684	12.956	0.005
2456267.69902	12.962	0.005
2456267.78586	13.035	0.006
2456267.78804	13.041	0.006
2456267.87890	13.058	0.005
2456267.88108	13.056	0.004
2456267.94838	13.024	0.005
2456267.95056	13.022	0.005
2456268.01312	13.001	0.006
2456268.01530	13.002	0.006
2456268.61656	12.995	0.004
2456268.61874	12.989	0.004
2456268.67150	12.994	0.004
2456268.67368	12.995	0.004
2456268.74206	13.007	0.004
2456268.74425	13.009	0.004

Table 3—Continued

Heliocentric Julian Date	V (mag)	$\sigma_V$ (mag)
2456268.81746	13.046	0.004
2456268.81964	13.052	0.004
2456268.88553	13.083	0.004
2456268.88771	13.090	0.004
2456268.95393	13.065	0.005
2456268.95611	13.060	0.005
2456269.01889	13.036	0.006
2456269.02107	13.021	0.006
2456269.58786	13.040	0.004
2456269.59004	13.036	0.004
2456269.66539	13.045	0.004
2456269.66757	13.049	0.004
2456269.74140	13.004	0.004
2456269.74358	13.000	0.004
2456269.82240	13.024	0.004
2456269.82457	13.018	0.004
2456269.85479	13.019	0.004
2456269.85697	13.016	0.004
2456269.93296	13.012	0.004
2456269.93514	13.014	0.004
2456269.99843	13.019	0.005
2456270.00061	13.013	0.005
2456270.58799	13.084	0.005
2456270.59017	13.093	0.005
2456270.65912	13.112	0.004
2456270.66130	13.113	0.004
2456270.72622	13.098	0.004
2456270.72840	13.100	0.004
2456270.79856	13.080	0.004
2456270.80074	13.084	0.004

Table 3—Continued

Heliocentric Julian Date	V (mag)	$\sigma_V$ (mag)
2456270.82714	13.092	0.004
2456270.82932	13.099	0.004
2456270.89863	13.100	0.004
2456270.90082	13.097	0.004
2456270.96193	13.096	0.005
2456271.58812	13.131	0.005
2456271.59029	13.120	0.005
2456271.65918	13.100	0.005
2456271.66136	13.105	0.005
2456271.72620	13.110	0.004
2456271.72838	13.111	0.004
2456271.80053	13.079	0.004
2456271.80271	13.079	0.004
2456271.83071	13.108	0.004
2456271.83289	13.105	0.004
2456271.89573	13.090	0.004
2456271.89791	13.089	0.004
2456271.95901	13.106	0.005
2456271.96119	13.096	0.005
2456272.58097	12.915	0.005
2456272.58315	12.911	0.004
2456272.63205	12.934	0.004
2456272.63423	12.929	0.004
2456272.68054	12.883	0.004
2456272.68272	12.880	0.004
2456272.74247	12.865	0.004
2456272.74465	12.870	0.004
2456272.79122	12.904	0.004
2456272.79340	12.911	0.004
2456272.83942	12.932	0.004

Table 3—Continued

Heliocentric Julian Date	V (mag)	$\sigma_V$ (mag)
2456272.84160	12.924	0.004
2456272.84863	12.923	0.004
2456272.85081	12.931	0.004
2456272.89251	13.003	0.004
2456272.89469	12.993	0.004
2456272.93692	12.984	0.004
2456272.93910	12.991	0.004
2456272.98148	12.991	0.004
2456272.98366	12.996	0.004

Table 4. CI Tau Orbital Properties and Inferred Mass of CI Tau b

Parameter	Using IR RVs	Using IR & Optical RVs
P (days)	$8.9965 \pm 0.0327$	$8.9891 \pm 0.0202$
K ( $\text{km s}^{-1}$ )	$1.084 \pm 0.250$	$0.950 \pm 0.207$
$e$	$0.40 \pm 0.16$	$0.28 \pm 0.16$
$M_p \sin i$ ( $M_{Jup}$ )	$8.81 \pm 1.71$	$8.08 \pm 1.53$
Fit RMS ( $\text{km s}^{-1}$ )	0.694	0.728



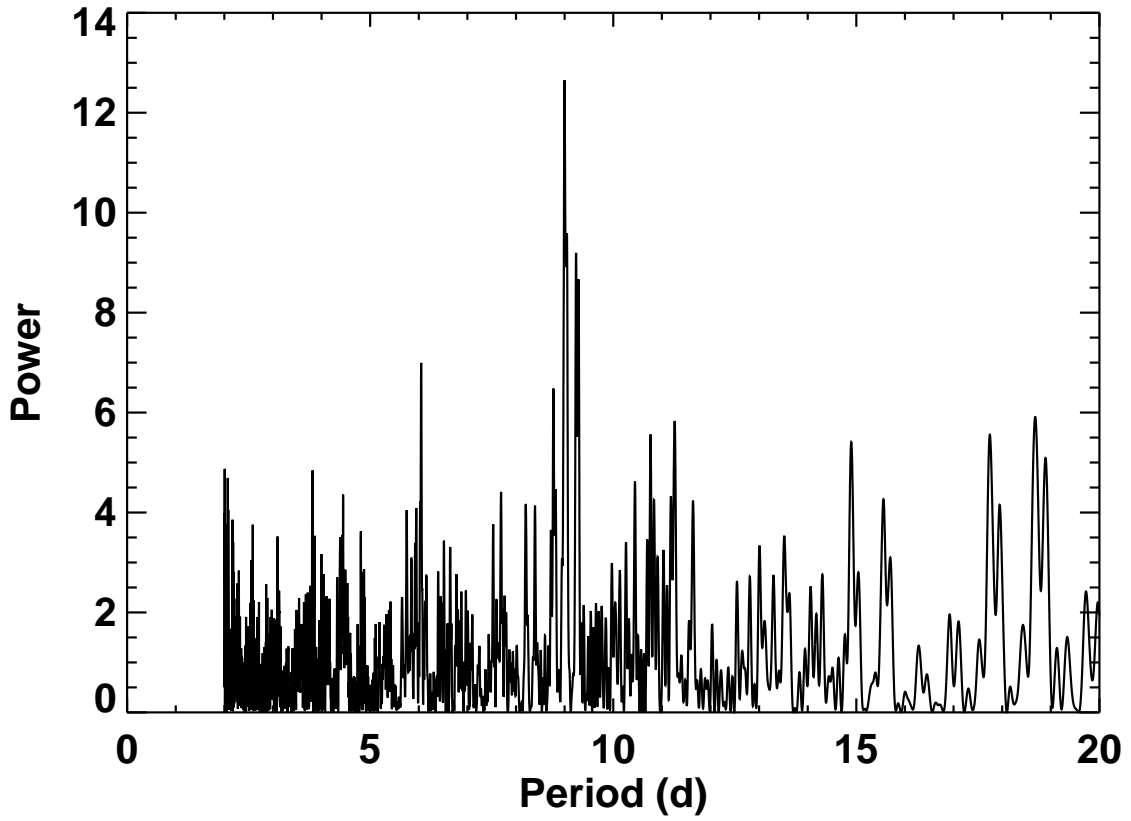


Fig. 1.— Power spectrum for the CI Tau IR spectroscopy based on multiple observations at different telescopes between 2009 November and 2014 November. **The strongest** peak appears with a 9 day period; the false alarm probability, calculated for these irregularly sampled data with a Monte Carlo simulation (see text), is 0.001.

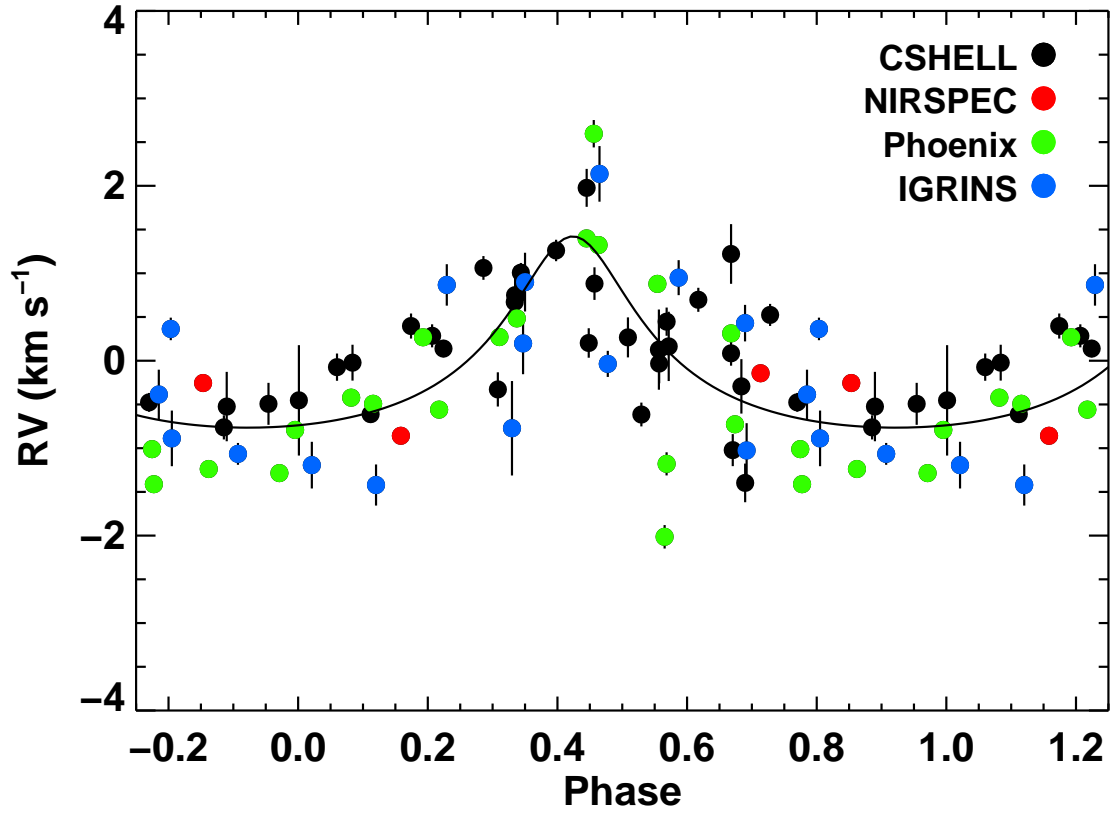


Fig. 2.— RVs for CI Tau based on all IR spectroscopy and phased to a period of 8.9965 days. The average RV has been subtracted from the data. Points are color coded to indicate the instrument used in the observations (Table 1)

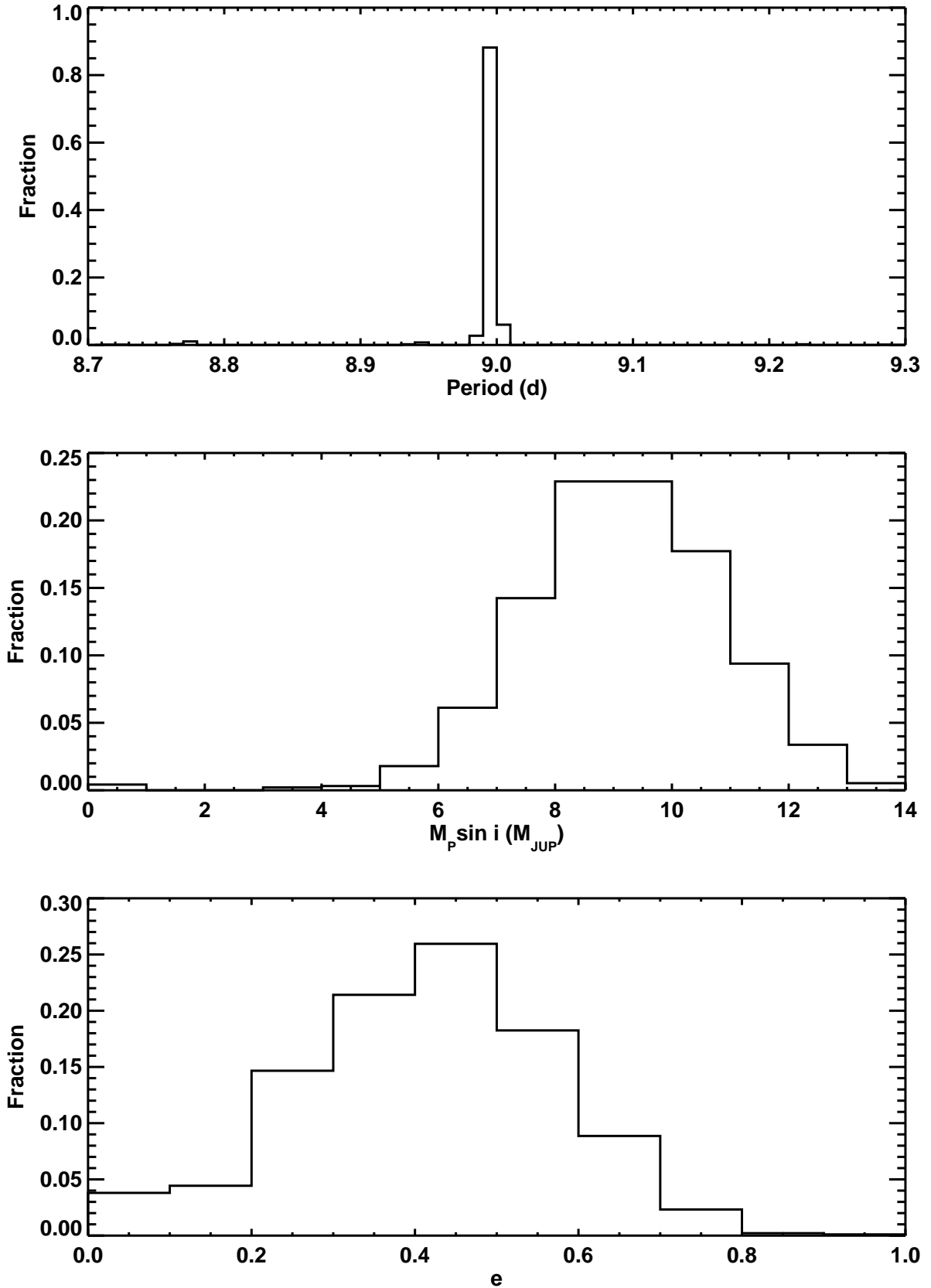


Fig. 3.— The distribution of recovered orbital properties based on the Monte Carlo simulation of the IR and BV data. The top panel shows the period, the middle panel

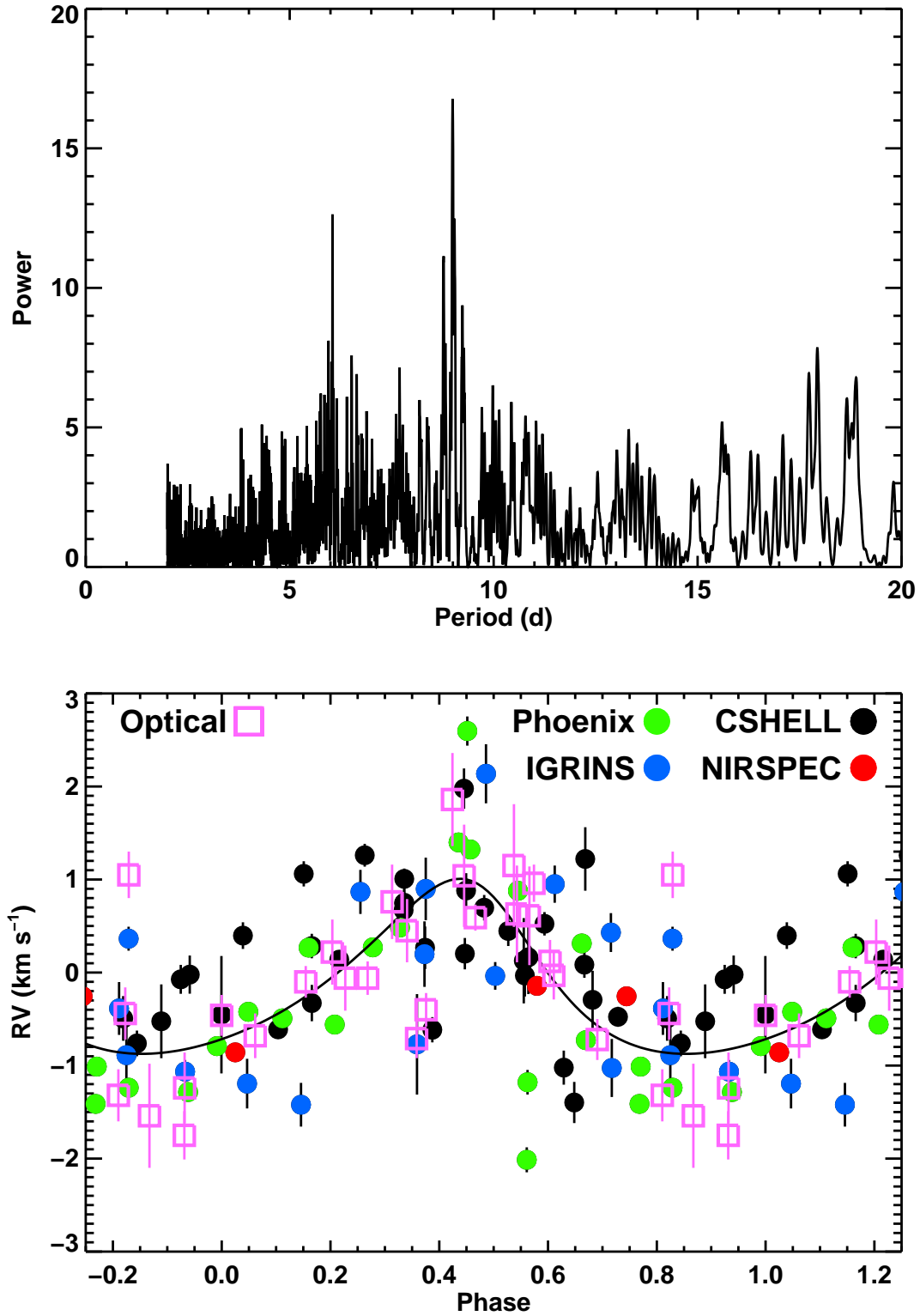


Fig. 4.— The upper panel shows the power spectrum of the combined optical and IR RV times series. The peak at  $\sim 9$  d has a false alarm probability of  $< 10^{-4}$ . The lower panel shows the IR and optical RV measurements phased to 8.99 d, determined from the combined RV time series.

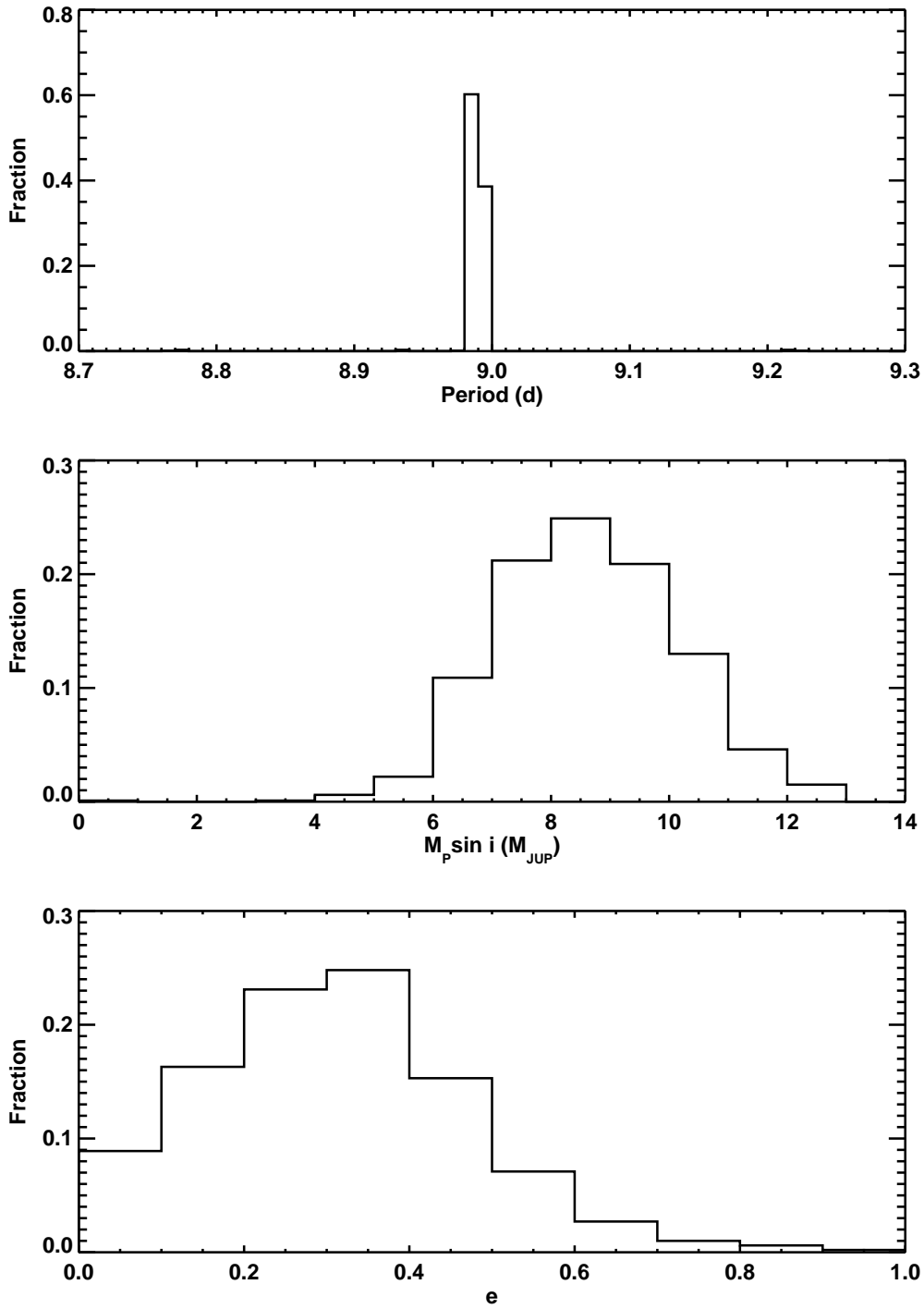


Fig. 5.— The distribution of recovered orbital properties based on the Monte Carlo simulation of the IR plus optical RV data. The top panel gives the recovered period, the middle panel gives the inferred planetary mass, and the bottom panel give the orbital eccentricity.

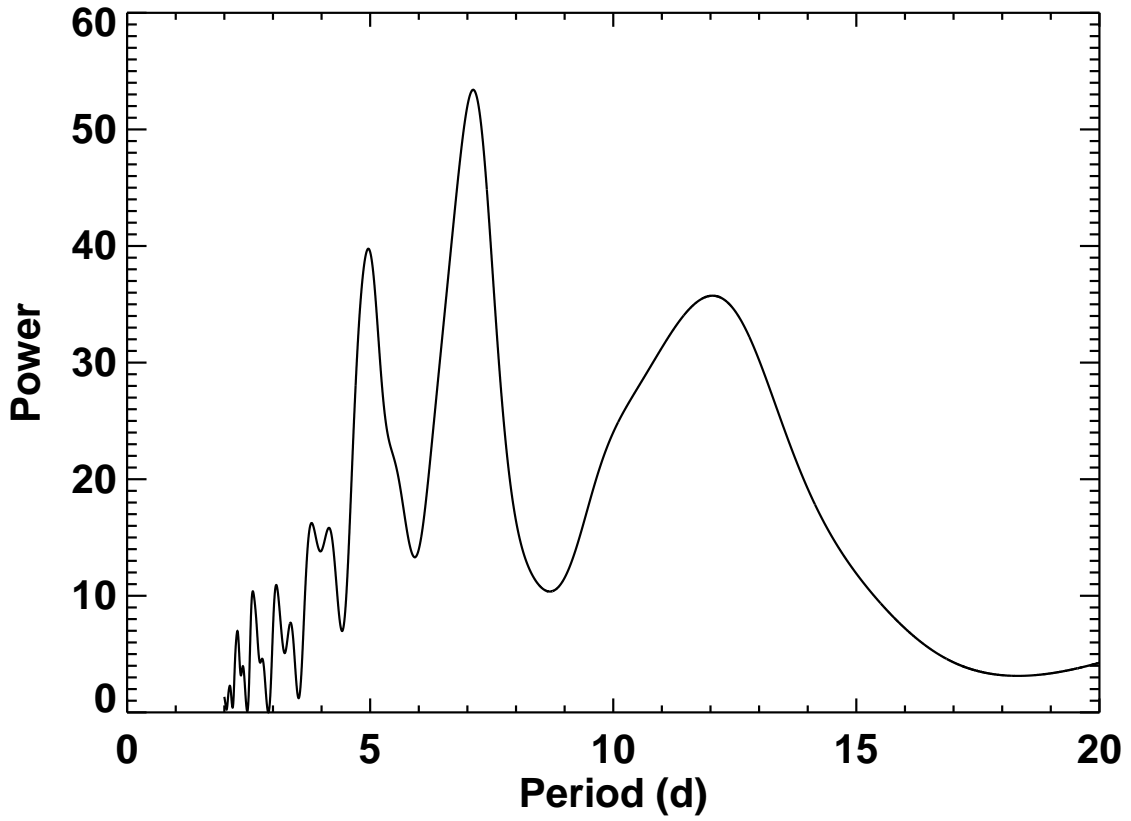


Fig. 6.— Power spectrum for the CI Tau optical photometry based on multiple observations per night (Table 1) over 14 nights in 2012 November and December. A clear peak appears with a 7.1 day period; the false alarm probability, calculated for these irregularly sampled data with a Monte Carlo simulation (see text), is  $< 10^{-4}$ .

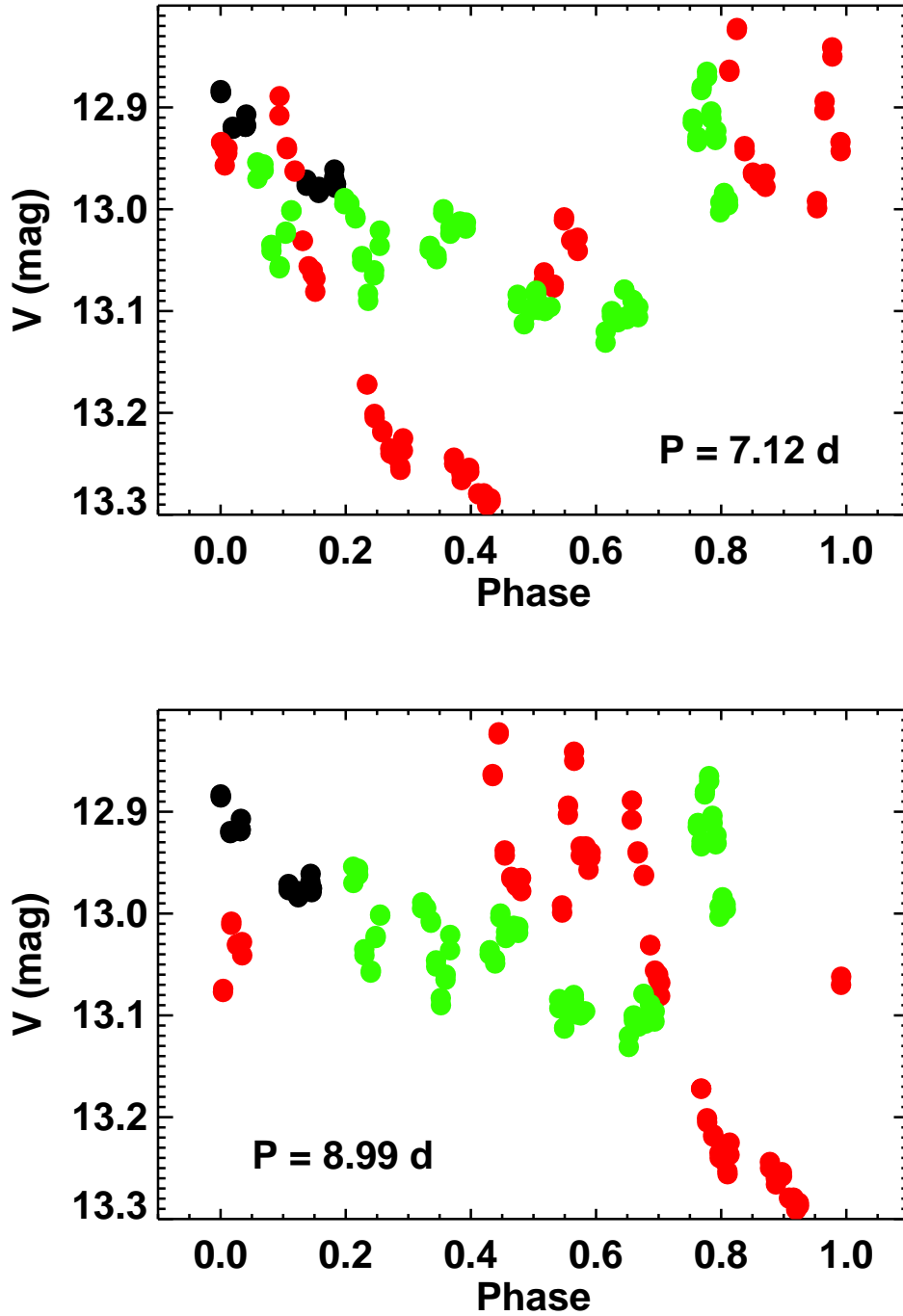


Fig. 7.— The upper panel shows the light curve showing the CI Tau V band photometry phased to period of 7.12 days. Uncertainties are smaller than the plot symbols. The black points are from the first observing run, red are from the second, and green from the third. The bottom panel shows the same data, only this time phased to a period of 8.99 days.

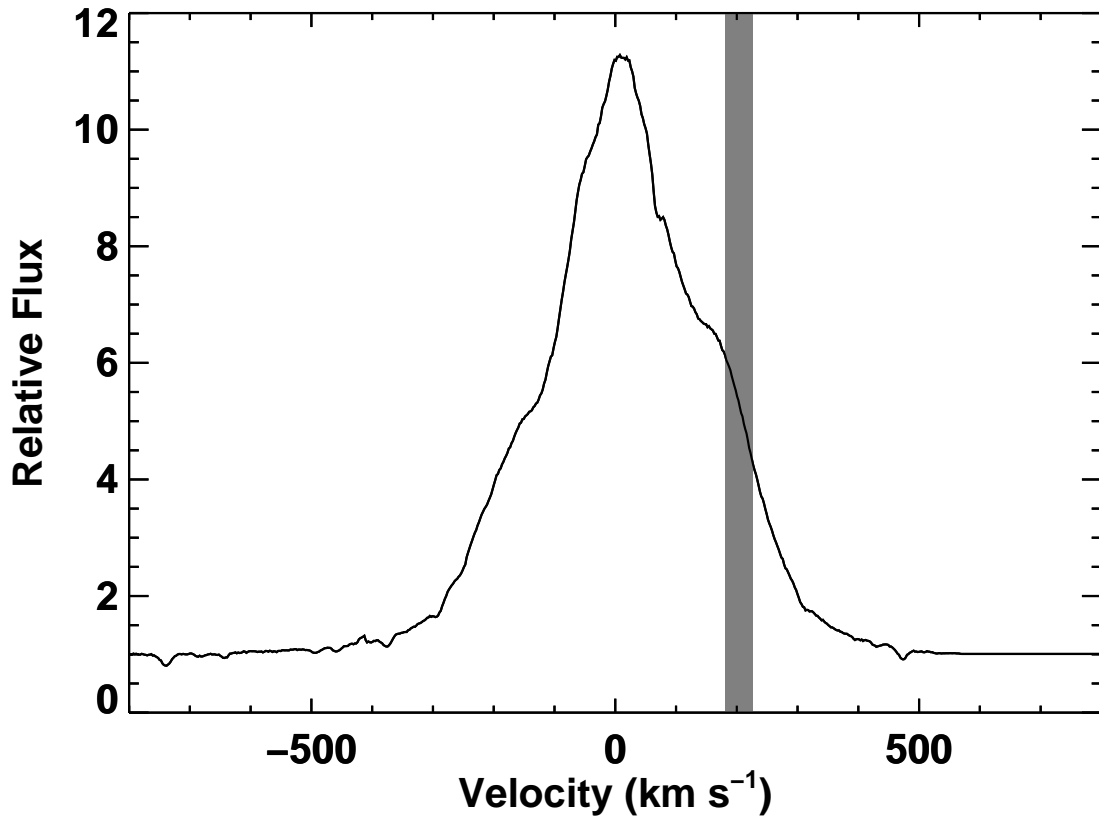


Fig. 8.— The mean H $\alpha$  line profile for CI Tau. The velocity range highlighted by the gray bar appears to show significant periodicity with a period near 9 d (see text).



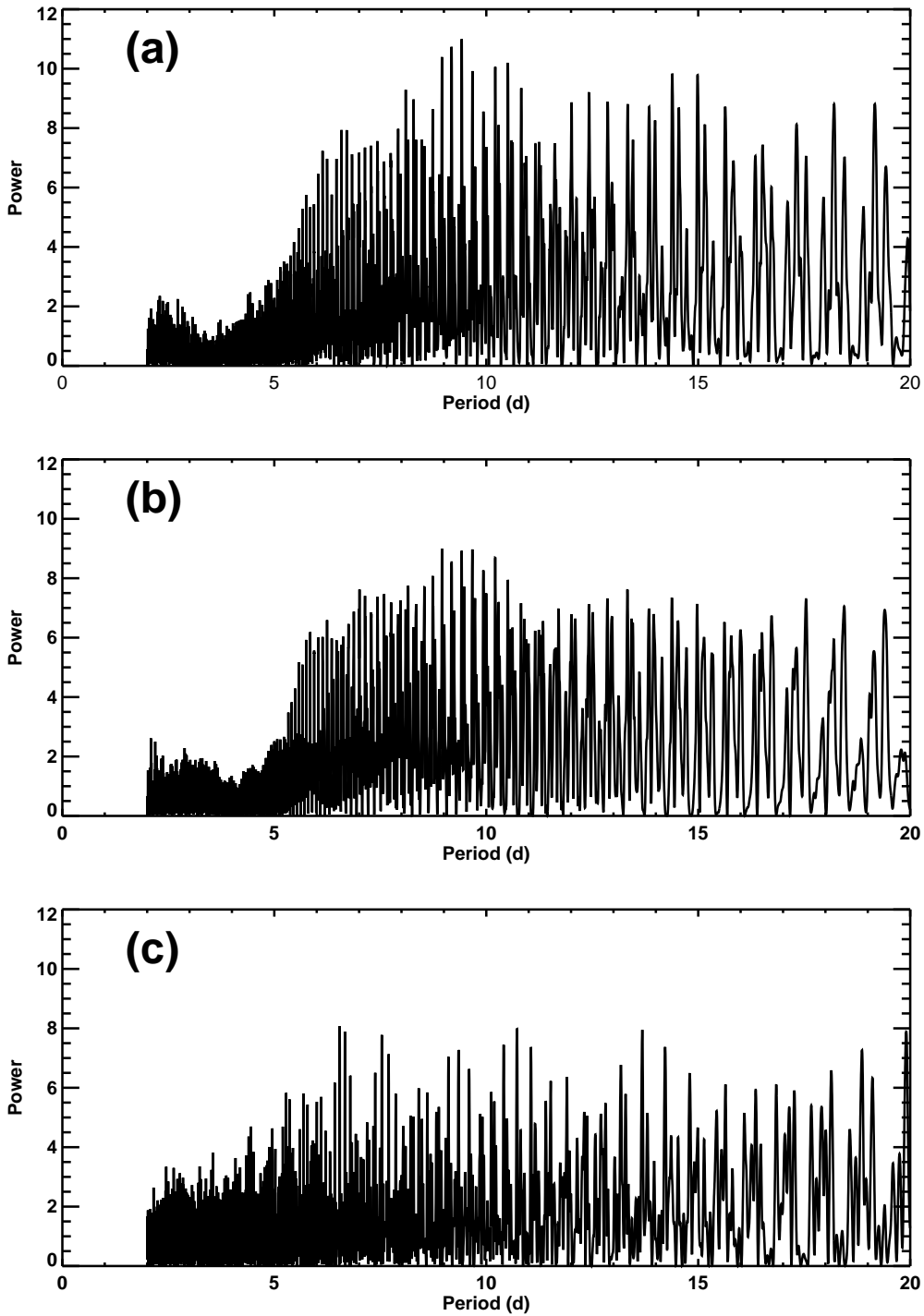


Fig. 9.— (a) The power spectrum of the H $\alpha$  velocity channel around  $\sim 200 \text{ km s}^{-1}$  showing the strongest power in the periodogram analysis. The 3 peaks from  $\sim 9.0 - 9.4 \text{ d}$  all have a false alarm probability  $< 10^{-4}$ ; however, they likely represent only one actual signal (see text). (b) and (c) The power spectra of the H $\alpha$  relative flux variations for the velocity channels around  $0 \text{ km s}^{-1}$  and  $-135 \text{ km s}^{-1}$ , respectively, showing the overall weakening of the power spectrum at other velocity channels.

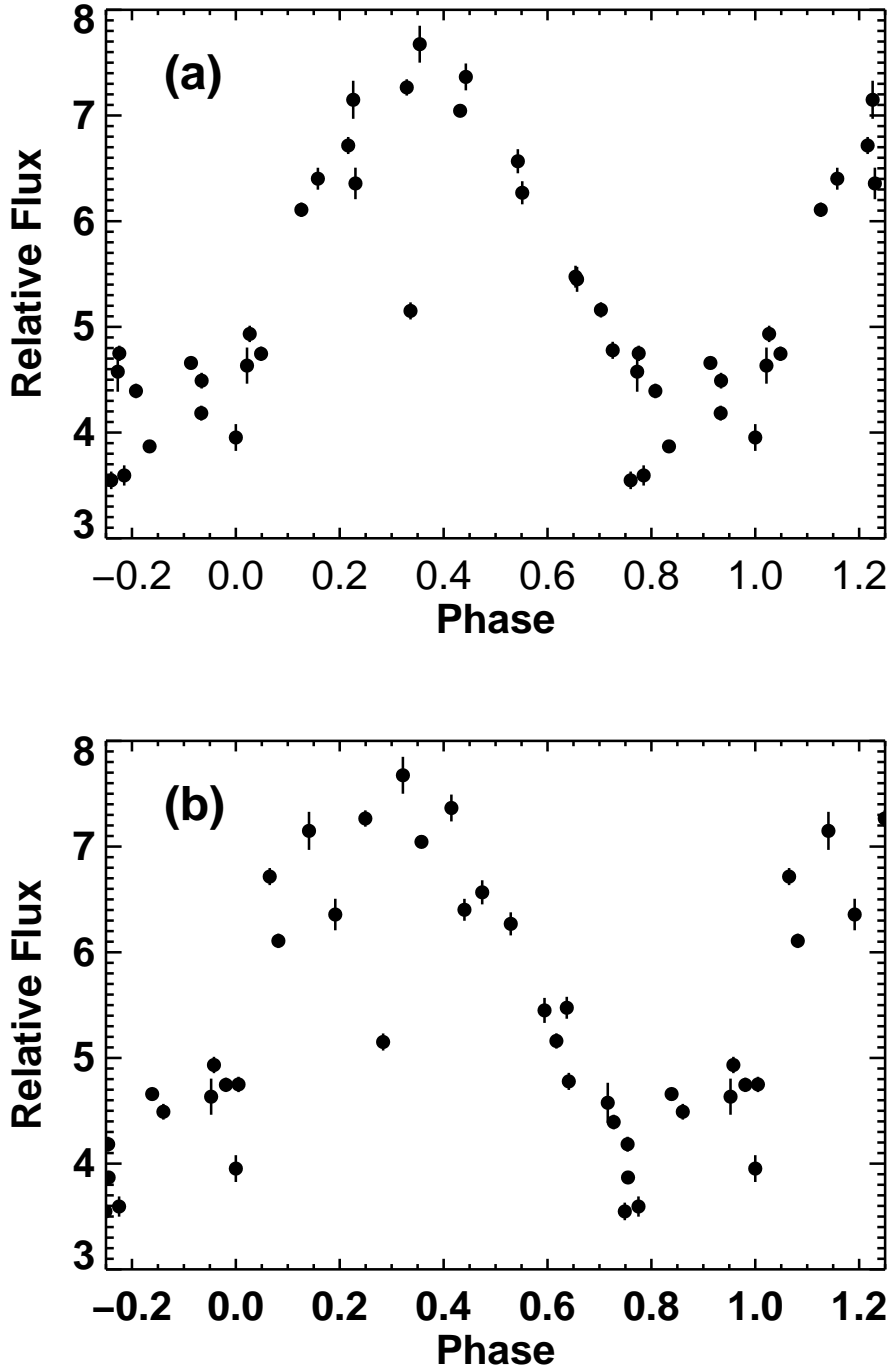


Fig. 10.— (a) The phased ( $p = 9.4$  d)  $H\alpha$  flux variation curve for the velocity channel showing the strongest power, shown in the periodogram in Figure 9a. (b) The phased  $H\alpha$  flux variation curve for the same velocity channel shown in Figure 9a but phased to  $p = 9.0$  d. The data phase well at this period also, indicating that we are not able to narrow down the true period beyond stating it is likely in the range 9.0 – 9.4 d.

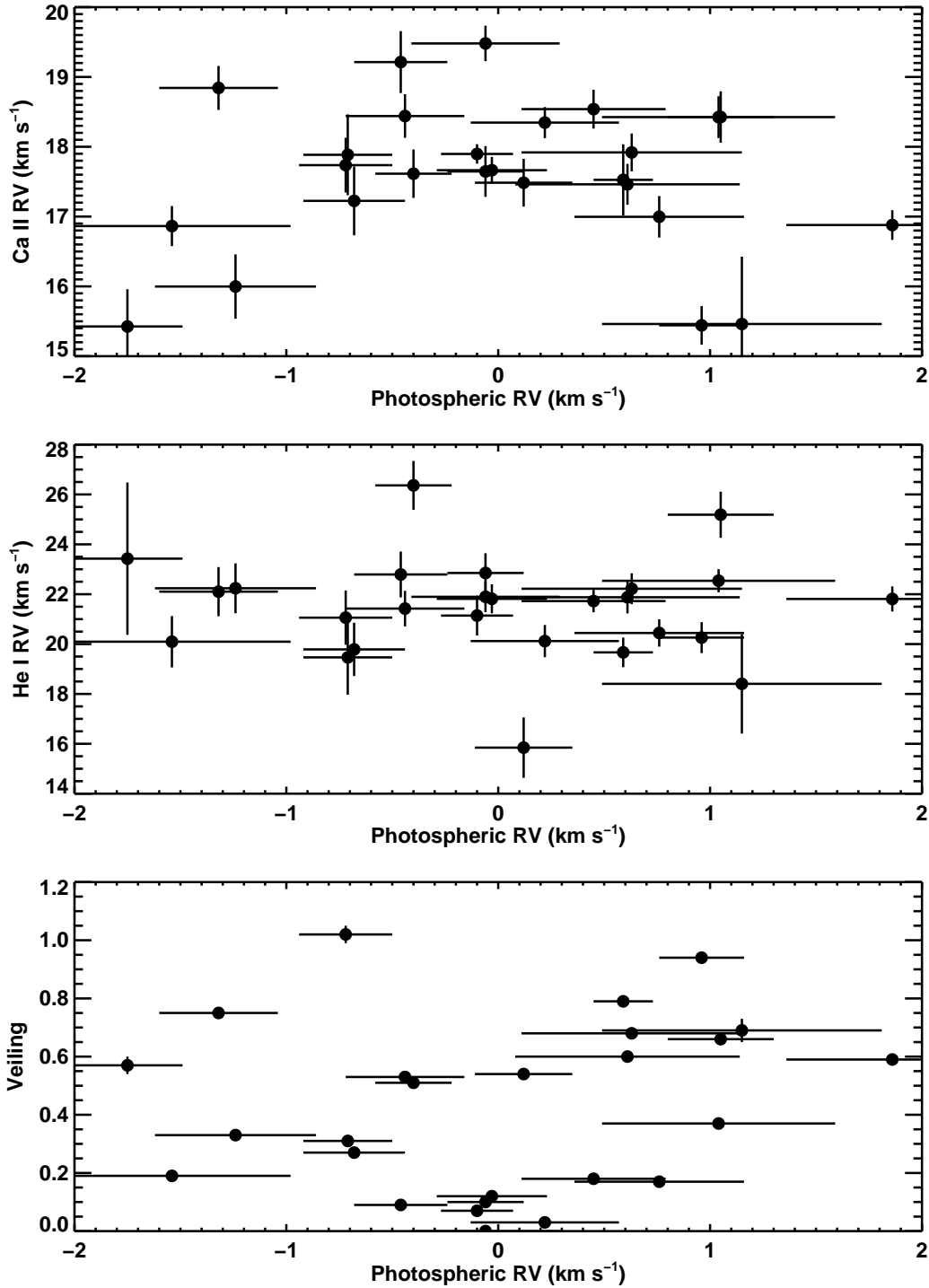


Fig. 11.— The top panel shows the Ca II 8662 Å RV measurements versus the photospheric RV measurements for the optical data. The middle panel shows the He I 5876 Å RV values versus the photospheric RVs, and the bottom panel shows the optical veiling versus the photospheric RV values. No significant correlation was found in any of these plots.

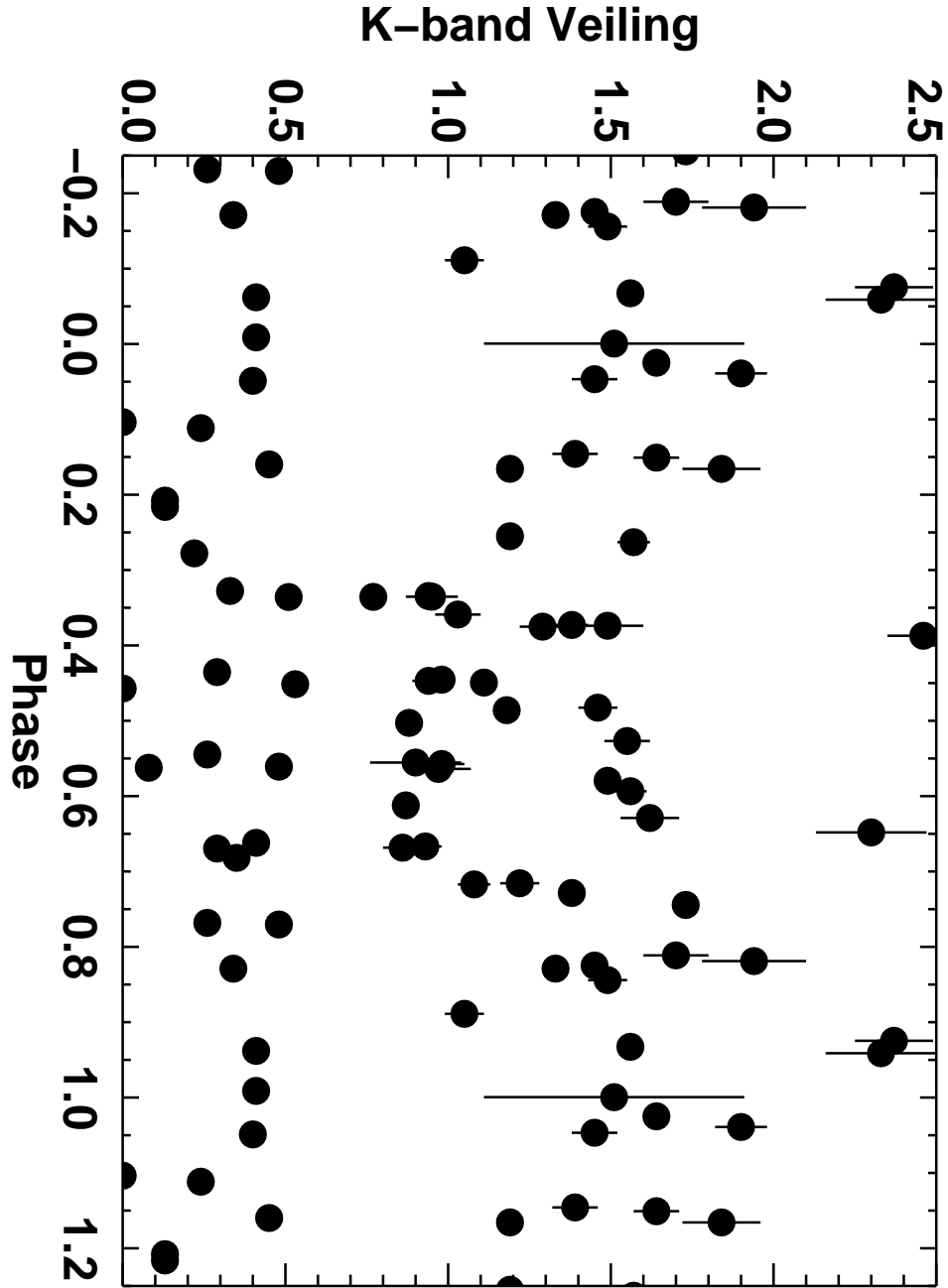


Fig. 12.— The K-band veiling versus phase determined from the combined optical plus IR RV fit (Figure 4).

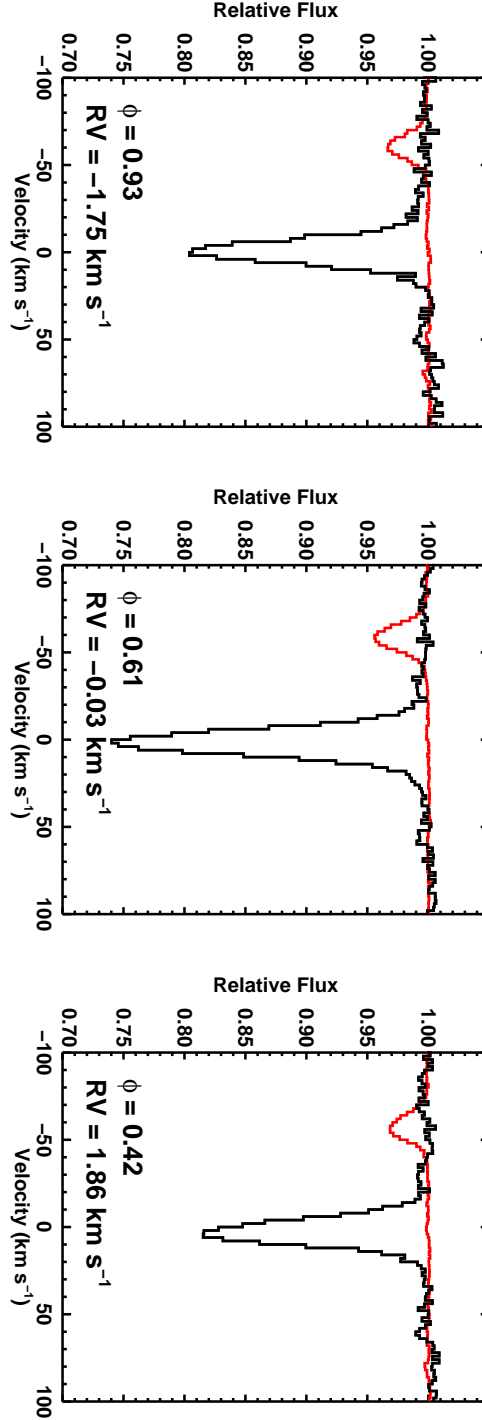


Fig. 13.— Three representative LSD profiles from the optical spectra, showing the observations with the smallest and largest measured RV as well as the observation closest to zero RV. The red profile shows the same profile offset by  $-60 \text{ km s}^{-1}$  and scaled to 17% to show the strength of the scattering feature needed to produce the measured RV variations (see text). The phase ( $\phi$ ) and RV of each observation is given.